TITLE

Post-transcriptional regulator HuR promotes immune evasion in pancreatic ductal adenocarcinoma

AUTHORS

Yifei Guo[1,2,3], Jennifer M. Finan[1,2,3], Alexandra Q. Bartlett[1,2,3], Shamilene Sivagnanam[2,3], Katie E. Blise[3], Nell Kirchberger[2,3], Konjit Betre[2,3], Grace A. McCarthy[1,2,3], Kevin Hawthorne[3,4], Canping Chen[5,6], Aaron Grossberg[3,7], Zheng Xia[5,6], Lisa M. Coussens[2,3], Rosalie C. Sears[3,4], Jonathan R. Brody[1,2,3], Robert Eil[1,2,3]

[1]Department of Surgery, Oregon Health & Science University, Portland, OR, USA;

[2]Department of Cell, Developmental & Cancer Biology, Knight Cancer Institute, Oregon Health & Science University, Portland, OR, USA;

[3]Brenden-Colson Center for Pancreatic Care, Knight Cancer Institute, Oregon Health & Science University, Portland, OR, USA;

[4]Department of Molecular and Medical Genetics, Oregon Health & Science University, Portland, OR, USA;

[5]Computational Biology Program, Oregon Health & Science University, Portland, OR, USA;

[6]Department of Biomedical Engineering, Oregon Health & Science University, Portland, OR, USA;

[7]Department of Radiation Medicine, Oregon Health and Science University, Portland, OR, USA.

RUNNING TITLE

HuR promotes immune evasion in pancreatic ductal adenocarcinoma

ACKNOWLEDGEMENTS

We would like to thank all members of the Brody laboratory and the Eil laboratory, the Brenden-Colson Center for Pancreatic Care, and the Knight Cancer Institute for their continued support and discussions regarding this work. This work was supported by the National Cancer Institute (NCI) of the National Institutes of Health (NIH) under awards R01 CA212600 (to J.R.B), U01 CA224012 (to R.C.S. & J.R.B), R21 CA263996 (to R.C.S. & J.R.B), and R01GM147365 (to Z.X.), K08 CA256179 (to R.E.), and P30 CA069533 (to L.M.C.), American Association for Cancer Research (AACR) under award 15-90-25-BROD (to J.R.B) and Transformative Oncology Research (to R.E.), the Hirshberg Foundation, and the

Brenden-Colson Center for Pancreatic Care, American Society of Clinical Oncology (ASCO) Career Development Award (to R.E.), PanCAN Career Development Award (to R.E.), America Cancer Society, the Susan G. Komen Foundation, the National Foundation for Cancer Research, and Hildegard Lamfrom Endowed Chair in Basic Research (to L.M.C.). We thank and acknowledge the invaluable work performed by members of the OHSU Research Cores and Shared Resources including members of the Flow Cytometry Core, Advanced Light Microscopy Core, and Histopathology Shared Resource. We thank the OHSU Department of Comparative Medicine for their support in animal care, especially Allie Buckner for her hands on care of our animals.

CONFLICT OF INTEREST

R.E. reports support from Lyell Immunopharma, and is a co-founder of VertaBio, Inc. L.M.C. has received reagent support from Cell Signaling Technologies, Syndax Pharmaceuticals, Inc., ZielBio, Inc., and Hibercell, Inc.; holds sponsored research agreements with Prospect Creek Foundation, grant support from Susan G. Komen Foundation, National Foundation for Cancer Research, and the National Cancer Institute; is on the Advisory Board for Carisma Therapeutics, Inc., CytomX Therapeutics, Inc., Kineta, Inc., Hibercell, Inc., Cell Signaling Technologies, Inc., Alkermes, Inc., NextCure, Guardian Bio, Dispatch Biotherapeutics, AstraZeneca Partner of Choice Network (OHSU Site Leader), Genenta Sciences, Pio Therapeutics Pty Ltd., and Lustgarten Foundation for Pancreatic Cancer Research Therapeutics Working Group, Inc.

AUTHOR CONTRIBUTIONS

Conceptualization: Y.G., J.R.B., R.E.; resource: A.G.; software: K.E.B., K.H., C.C.; formal analysis: Y.G., K.E.B., S.S., K.H., C.C.; supervision: A.G., Z.X., L.M.C., R.C.S., J.R.B., R.E.; funding acquisition: A.G., Z.X., L.M.C., R.C.S., J.R.B., R.E.; investigation: Y.G., J.M.F., A.Q.B., S.S., N.K., N.B., G.A.M.; visualization: Y.G., S.S.; writing – original draft: Y.G., J.R.B., R.E.; writing – review & editing: Y.G., J.M.F., A.Q.B., S.S., K.E.B., L.M.C., R.C.S., J.R.B., R.E..

ABSTRACT

The tumor microenvironment (TME) of pancreatic ductal adenocarcinoma (PDAC) is characterized by a limited infiltration of tumor-specific T cells and anti-tumor T cell activity. Extracellular factors in the PDAC TME have been widely reported to mediate immune suppression, but the contribution from tumor-intrinsic factors is not well understood. The RNA-binding protein, HuR (*ELAVL1*), is enriched in PDAC and negatively correlates with T cell infiltration. In an immunocompetent Kras-p53-Cre (KPC) orthotopic model of PDAC, we found that genetic disruption of HuR impaired tumor growth due to a novel role of HuR inducing T-cell suppression. Importantly, we found that HuR depletion in tumors enhanced both T cell number and activation states and diminished myeloid phenotypes by comprehensive spatial profiling of the PDAC TME. Mechanistically, HuR mediated the stabilization of mTOR pathway transcripts, and inhibition of mTOR activity rescued the impaired function of local T cells. Translating these findings, we demonstrated that HuR depletion sensitized PDAC tumors to immune checkpoint blockade, while isogenic, wildtype tumors are resistant. For the first time, we show that HuR facilitates tumor immune suppression in PDAC by inhibiting T cell infiltration and function and implicate targeting HuR as a potential therapeutic strategy in combination with immunotherapy.

SIGNIFICANCE

This study identified a novel mechanism that HuR supports pancreatic tumor growth by restricting T cell infiltration, promoting immune evasion. Our work supports targeting strategies against HuR in PDAC with the goal of enhancing PDAC sensitivity to immune-based cancer therapies, such as checkpoint blockade and T cell transfer.

71 **INTRODUCTION**

72 Pancreatic ductal adenocarcinoma (PDAC) is one of the leading causes of cancer-related death worldwide with a 5-
73 year survival rate of 13%, underscoring the need to develop improved therapeutic strategies[1]. The complex tumor
74 microenvironment (TME) of PDAC is thought to hinder both chemo- and immunotherapy efficacy[2]. Despite the presence
75 of immunogenic neoantigens that are predicted to be recognized by endogenous T cells, PDAC has remained resistant
76 to immune checkpoint blockade (ICB)[3–5]. Some have proposed that the ability of cancer cells to downregulate antigen
77 presentation machinery is a major driver of evading T cell recognition in PDAC. However, only a small proportion (~1-2%)
78 of PDAC contain mutations within antigen presentation or processing machinery[6]. Even in patients with mismatch repair
79 deficient (MMR-D) driven PDAC, where neoantigen frequency is equivalent to other MMR-D cancers, ICB had
80 compromised rates of objective response in PDAC in comparison to other MMR-D cancers[7]. Thus, we and others have
81 concluded that unresolved tumor-intrinsic sources of T cell suppression exist in PDAC. Specifically, cytotoxic T cells in the
82 PDAC TME have characteristics of T cell dysfunction, such as an inadequate response to stimulation (hypo-responsiveness),
83 which is recognized as a major source of tumor immune escape[8–10]. Therefore, in PDAC, there remains a need to understand
84 and reverse the tumor specific mechanisms that drive resistance to cancer immunotherapies[11].

85 Investigators continue to appreciate that TME features, including cytokines and cell-cell interactions, can restrain
86 the antitumor functions of $CD4^+$ and $CD8^+$ T cells. In tumors, PDAC especially, a combination of rapid cellular proliferation
87 and pathologic extracellular architecture contribute to a microenvironment that is low in both glucose and oxygen[12,13].
88 Meanwhile, T cells depend on consumption of nutrients to effectively respond to TCR ligation with acquisition of effector
89 programs, production of cytokines, and target cell cytolysis. Thus, the tumor-imposed nutrient deficit results in a metabolic
90 competition with local immune cells, contributing to T cell hypo-responsiveness and resistance to immunotherapies[14]. As
91 others have increasingly appreciated the importance of nutrient availability and metabolism for effective T cell antitumor
92 function, interest continues to grow in therapies that could increase nutrient availability and consumption by tumor-specific
93 T cells[15].

94 In human PDAC and preclinical models, the RNA-binding protein, human antigen R (HuR, *ELAVL1*) is known to
95 be hyperactive, supporting multiple programmatic hallmarks of cancer[12,13,16,17]. Functionally, HuR recognizes and binds to
96 3' untranslated regions (UTRs) of transcripts, enhancing their stability and translation[18]. For instance, HuR reshapes the
97 metabolic profile of PDAC, in part, by stabilizing *IDH1* transcripts and reprogramming both glycolytic and
98 lipogenic metabolism[13,19,20]. Broadly, HuR activity is associated with Myc programs and glycolytic metabolism, enhancing

99 the activation of c-Myc programs and consumption of surrounding nutrients for growth in size and cell division[12,21,22].
100 Additionally, pancreas-specific HuR overexpression alone caused fibro-inflammation in the mouse pancreas and led to an
101 increase in precursor lesions of PDAC in cooperation with a *Kras*^{G12D} mutation[23]. Our prior observations support a model
102 wherein tumor-intrinsic HuR can mediate cell-cell communication and alter the PDAC TME in immune compromised
103 models[13,24]. In the context of metabolic competition between tumor and immune cells, we hypothesized that tumor-intrinsic
104 HuR activity may drive a competitive metabolic advantage over neighboring T cells. Yet, due to a lack of murine PDAC
105 model that can capture the immune contexture with HuR depletion, the role of HuR in the PDAC-immune crosstalk has not
106 been examined[16,17,24].

107 Taken together, our prior works point to a hypothesis that HuR may have a substantial role in mediating immune
108 evasion in the PDAC TME. Moreover, we report here that HuR expression is negatively correlated with both T cell
109 infiltration and outcome in PDAC patients. Thus, we investigated whether depletion of HuR in PDAC would impact tumor
110 growth and anti-tumor immune activity in an immunocompetent model of PDAC. To this end, we developed an isogenic
111 *Kras*^{G12D}*,Trp53*^{R172H}*,Pdx1-Cre* (KPC) mutant-driven murine PDAC model, with and without HuR, to further elucidate the
112 impact of tumor-intrinsic HuR on the immune components of the PDAC TME[25]. We observed that tumors with disruption
113 in the *Elavl1* locus (HuR) had impaired tumor growth *in vivo.* We then assayed the tumors with multiplex
114 immunohistochemistry (mIHC)[26], a single-cell spatial proteomics imaging technology, and subsequently used machine
115 learning to unbiasedly detect the main differences in TME immune contexture between tumors with HuR versus tumors
116 without HuR. We found that HuR-deficient KPC tumors were most distinctly characterized by their increased infiltration of
117 CD4$^+$ T cells and increased frequency of spatial proximities involving anti-tumoral "M1-like" CD206$^-$ macrophages and
118 CD4$^+$ T cells, while HuR-competent KPC tumors possessed an immunosuppressive, myeloid-enhanced spatial phenotype.
119 Moreover, antibody-based depletion of CD4$^+$ and CD8$^+$ T cells restored the *in vivo* growth of HuR-deficient KPC tumors,
120 demonstrating that HuR is required for intact PDAC growth in the immunocompetent setting. Introduction of a model
121 antigen and assessment of tumor specific T cells identified that tumor-intrinsic HuR deterred the infiltration of antigen-
122 specific CD8$^+$ T cells and their acquisition of effector functionality. Mechanistically, HuR mediated stabilization of mTOR
123 pathway-related transcripts and enhanced PDAC nutrient consumption to the detriment of local T-cell antitumor function.
124 Consistent with such a model, inhibition of the mTOR pathway in PDAC cells enhanced the cytokine production capacity
125 of co-cultured CD8$^+$ T cells in an HuR-dependent manner. Therapeutically, KPC tumor's resistance to ICB treatment was

126 dependent on the presence of HuR, and HuR depletion combined with ICB led to tumor regression. Herein, we provide a
127 deeper understanding of a potent immune suppression mechanism driven by the pro-oncogenic protein, HuR, in PDAC.
128

129 **METHODS**

130 *HuR signature scoring of RNA-seq OPTR cohort and survival analysis*

131 Expression of the HuR activity signature[17] was assessed for 218 primary PDAC tumor RNA-seq profiles from the
132 Oregon Pancreas Tissue Registry (OPTR) cohort described in Link JM et al.[27]. Pseudoaligned transcript abundances for
133 each RNA-seq profile were summed to gene level using tximport[28] and subsequently used as input for DESeq2[29]. Gene
134 expression values were transformed with DESeq2 variance-stabilizing transformation (VST). The GSVA[30] algorithm was
135 then applied to VST count data to assign HuR signature scores to each sample. Overall survival was assessed in the same
136 208 patients described previously[27] but filtered by HuR signature scores. Patients were stratified into groups representing
137 high HuR signature expression (GSVA score in the top quartile) and low (GSVA score in the bottom quartile). Survival was
138 compared using the survival[31] and survminer[32] packages.
139

140 *Single-cell data collection and analysis*

141 Single-cell RNA sequencing (scRNA-seq) data were sourced from the Deeply Integrated Single-Cell Omics
142 (DISCO) database[33]. A total of 115 PDAC samples, encompassing 557,304 cells, were utilized to investigate the relationship
143 between *ELAVL1* gene expression in malignant cells and lymphocyte infiltration. Malignant cells were identified using the
144 R package scATOMIC (v2.0.2)[34] with the parameter "known_cancer_type = PAAD cell" and default settings for other
145 parameters. Spearman's correlation analysis was conducted to assess the association between gene expression levels in
146 tumor cells and cell-type infiltration in each sample.
147

148 *Immunohistochemistry staining of tumors*

149 Mouse tissues were fixed in 4% PFA overnight at 4°C before embedding and 5 µm sectioning. As previously
150 described[24], paraffin-embedded histological sections were stained for HuR (Santa Cruz Biotechnology; sc-5261) overnight
151 at 4°C, followed by incubation with a biotinylated secondary antibody for 1 hour at room temperature. Color was developed
152 with DAB substrate (Vector Laboratories; SK-4100), and mount for imaging. Brightfield images were acquired by Zeiss
153 Axio slide scanner.

154

155 *Cell lines and virus*

156 The PDAC murine cell line, KPC8069 ($Kras^{G12D}$-$Trp53^{R172H}$-Pdx1Cre), was a gift from Dr. Michael Hollingsworth.
157 Cells were cultured in normal DMEM with 10% fetal bovine serum (Gibco) and 1% penicillin/streptomycin (Thermo
158 Scientific; 15070063). Cell lines were maintained at 37°C in 5% humidified CO_2. Cell lines were *Mycoplasma* tested
159 routinely using Mycoplasma Detection Kit (SouthernBiotech; 13100-01). Before any experiment, cells were passaged at
160 least twice after thawing.

161 For HuR re-expression, KPC8069 cells were transfected with ecotropic retrovirus either carrying codon-enhanced
162 *Elavl1* sequence or empty vector and supplemented with 1 μg/ml polybrene (Millipore Sigma; TR1003G). Cells containing
163 the target vectors were selected by hygromycin (Millipore Sigma; H3274) and validated for HuR expression with
164 immunoblotting. For ovalbumin (OVA) expression, KPC8069 cells were transfected with ecotropic retrovirus carrying the
165 full-length OVA sequence and supplemented with 1 μg/ml polybrene. Cells containing the target vectors were selected by
166 blasticidin (Alfa Aesar; J67216-XF) and validated for OVA expression with flow cytometry.

167 All ecotropic retroviruses are generated by packaging 20 μg of plasmid DNA synthesized by Genscript, Inc.
168 containing genes of interest in an MSCV derived γ-retrovirus backbone (derived from Addgene; 122727) along with 3 μg
169 pCL-Eco plasmid DNA (Addgene; 12371) with platinum-E ecotropic packaging cells (Cell Biolabs; RV-101) and
170 jetOPTIMUS transfection reagent (Avantor; 101000006).

171

172 *INDEL assessment*

173 For INDEL assessment, genomic DNA was harvested from cells at time of analysis using the DNeasy Blood and
174 Tissue DNA kit (Qiagen; 69504), and the region containing *Elavl1* short guide (sg) RNA target was PCR-amplified and
175 Sanger sequenced by Eurofins Genomics. For each sample, a 493-bp region was amplified for sequencing (forward primer:
176 5′-ACTGGGGCTGAAGAAAAGTAGT-3′, reverse: 5′-GAACTGAATCATCTCCCCGGT-3′). 100 to 200 ng of each
177 amplicon was sent for sequencing with 2 pmol of its respective sequencing primer (5′-
178 TAGTCTGAGGTTAAAGAACAAAACTTCATT-3′). The indel percentage of amplicons derived from HuR-KO cells was
179 deduced using the Synthego ICE tool (Synthego; ICE Analysis v3.0).

180

181 *Immunoblot analysis*

182 Cells were lysed using ice-cold RIPA buffer (Thermo Scientific; 89900) supplemented with protease inhibitors
183 (Thermo Scientific; 87786). Protein concentration was quantified using the Pierce BCA Protein Assay kit (Thermo
184 Scientific; 23225). Equal amounts of whole protein extracts were loaded and separated by electrophoresis on a 4% to 12%
185 Bis-Tris gel (Invitrogen; NP0321BOX) and transferred to a PVDF membrane (Bio-Rad; 1704156). Blots were blocked in
186 Intercept® (TBS) Blocking Buffer (LI-COR Biosciences; 927-70003) and then probed with antibodies against anti-HuR
187 (1:1000, Santa Cruz Biotechnology; sc-5261) and anti-α-tubulin (1:5000, Invitrogen; A11126), followed by Thermo Fisher
188 Scientific Alexa secondary antibodies. Immunofluorescence was measured using a digital imager (Invitrogen; iBright 1500).
189

190 *RNA extraction and RT-qPCR*

191 RNA was extracted using RNeasy Mini Kit (Qiagen; 74106). RNA concentrations and quality were assessed by
192 NanoDrop spectrophotometer (Thermo Scientific). Complementary DNA (cDNA) was made from 500 ng RNA using High
193 Capacity cDNA Reverse Transcriptase Kit (Thermo Scientific; 4368813). RT-qPCR was performed with SYBR green
194 master mix (Thermo Scientific; 4385617) with HuR primers and cDNA. Amplification signal was captured by RT-qPCR
195 machine (Thermo Scientific; QuantStudio 7 Flex). Relative quantifications were assessed using the Log_2–ΔΔCt method,
196 using GAPDH for normalization.
197

198 *Mouse experiments*

199 Animal protocol # IP00003322 and #IP00003155 were approved by Institutional Animal Care Regulations and Use
200 Committee of OHSU. These protocols are specifically applicable to the experiments reported in this manuscript. All mice
201 were obtained from The Jackson Laboratory. C57BL/6 mice (Cat. 000664) of 8–9 weeks of age were used as recipient hosts
202 for KPC tumor implantation. OT-I transgenic mice were used as OT-I T cell donors.

203 For T cell depletion studies, mice were intraperitoneally injected with αCD8 blocking antibody (200 μg, BioXcell;
204 BE0061) and αCD4 blocking antibody (200 μg; BioXcell; BE0003-1) two days before tumor implantation. The treatment
205 was maintained for the duration of the experiment by injecting every four days of αCD8 and αCD4 (100 μg each). For
206 isotype controls, rat IgG2b (BioXcell; BE0090) at matching amount was used. This approach achieved >99% depletion of
207 $CD8^+$ and $CD4^+$ T cells in spleens of T cell-depleted mice compared to control mice at endpoint.

208 For αPD-1 treatment, mice were intraperitoneally injected with αPD-1 blocking antibody (200 μg, BioXcell;
209 BP0146) or isotype controls, rat IgG2a (BioXcell; BE0089) every 4 days. The first injections happened 5 days after tumor
210 implantation, and each mouse received a total of 4 injections.
211
212 *Mouse PDAC tumor model*
213 For implantable tumor experiments, KPC tumor cells (1×10^6) were resuspended in 100 μl of 1:1 mixture of PBS
214 (Fisher Scientific; 14-190-250) and Matrigel (Fisher Scientific; 354234), injected subcutaneously into the flanks of mice,
215 and allowed to grow for 37 days. Tumor length and width were measured by caliper every four days.
216 For orthotopic tumor growth experiments, KPC tumor cells (4×10^4) were resuspended in 20 μl of 1:1 mixture of
217 PBS and Matrigel, orthotopically injected into the tail of mouse pancreas, and allowed to grow for 20 days. For orthotopic
218 tumor αPD-1 experiments, KPC tumor cells (9×10^4) were injected and allowed to grow for 15 days. Earlier endpoint
219 criteria included severe weight loss, or extreme weakness and inactivity. Tumor weight was measured by chemical scale
220 (Sartorius) at the endpoint.
221
222 *Flow cytometry and analysis*
223 Following euthanasia, tumors and spleens were promptly dissected, weighed, and stored in ice-cold PBS. Tumors
224 were subsequently minced with surgical scissors and dissociated with GentleMACS octo-dissociator and preset program
225 (m_impTumor_01, Miltenyi Biotec). The dissociated tumor was then filtered through a 40 μm filter. Spleens were mashed
226 and filtered through a 40 μm filter. All samples were ACK lysed for 60 seconds using ACK lysing buffer (Gibco; A1049201),
227 and then consolidated for staining.
228 Single-cell suspension of each sample was incubated with Live/Dead Fixable Aqua (Thermo Scientific; L34966)
229 and Fc block (BD; 553142) in PBS for 30 min at 4°C, followed by incubation with primary fluorochrome-labeled antibodies
230 at 4°C for 30 min in PBS with 0.5% BSA and 2 mM EDTA. For *ex vivo* cytokine production by T cell, samples were
231 incubated for 4 hours at 37°C with PMA (20 ng/mL, Sigma; P1585), ionomycin (1 μg/mL, Sigma; I0634), and GolgiStop
232 (BD; 554724). Intracellular staining was done using the Fixation/Permeabilization Kit (BD; 554722). Antibodies used in
233 flow analysis are listed in Supplementary Table 1. Flow cytometric analysis was performed on Cytek Aurora spectral
234 cytometer. Collected data were analyzed using FlowJo v10 (TreeStar).
235

236 *mIHC image acquisition and analysis*

237 As previously described[10,35,36], multiplex staining was performed on 5 μm sections and each stained image was
238 scanned at 20× magnification on an Aperio AT2 scanner (Leica Biosystems). The antibody panel used consisted of lineage
239 markers and phenotype markers (Supplementary Table 2). Multiple 2.0 mm^2 tissue regions were sampled from each tumor,
240 resulting in 31 total tissue regions across 8 tumors. Tissue regions were registered using Matlab Computer Vision Toolbox
241 (The Mathworks, Inc.), color deconvolution was performed using ImageJ, and nuclei segmentation was performed using
242 StarDist. Single-cell mean intensity for each stain was quantified using Cell Profiler[37]. Single biomarker positivity
243 thresholds were set using FCS Express Image Cytometry RUO (De Novo Software). Single-cell classification was
244 performed using R Statistical Software according to the defined phenotypic gating hierarchy (Supplementary Table 3).

245

246 *mIHC spatial quantifications*

247 The spatial organization of cells within tissue regions was quantified via cell-cell spatial proximities and recurrent
248 cellular neighborhoods (RCNs), as previously published[10]. Cell-cell spatial proximities were calculated by counting the
249 frequency at which two cell types occur within 20 μm of each other, then dividing the count by the summed densities of the
250 two cell types involved in the proximity per tissue region. This normalization was used to mitigate the effect of cells present
251 in high densities. RCNs were calculated by first identifying neighborhoods for every cell present across all tissue regions.
252 Neighborhoods were defined by counting all cells within a 60 μm radius from the given seed cell. 76 cells had no
253 neighboring cells within 60 μm and were dropped from the RCN analysis. The remaining 429,602 cells across the dataset
254 were grouped using k-means clustering according to the normalized phenotypic composition of their neighborhood. The
255 elbow method was used to determine the optimal number of groups to cluster the cell neighborhoods into. This resulted in
256 each cell being assigned to one of eight RCNs, and the proportions of RCNs present per tissue region were calculated.
257 Previously published code[10] was used to complete the spatial analyses using Python software and the following packages:
258 pandas, numpy, scipy, and scikit-learn.

259

260 *Machine learning pipeline*

261 Following the previously published pipeline[10], an elastic net model was trained to classify samples based on tumor
262 genotype (*scramble* vs *sgElavl1*). Input features to the model included 12 cell population densities, 78 cell-cell proximity
263 frequencies, and 8 RCN proportions, resulting in 98 total TME features calculated for each of the 31 tissue regions. Features

264 were log10+1 transformed and scaled from zero to one to improve model interpretability. Predictions were made on a tissue
265 region basis to maximize sample size and provide the model with the greatest amount of data to learn biologically relevant
266 patterns. A leave-one-tumor-out cross-validation approach was used to prevent data leakage between cross-validation folds,
267 and model hyperparameters remained the same across folds to prevent artificial inflation of performance. Briefly, for each
268 fold, a new model was trained from tissue regions from seven of the eight tumors, while tissue regions from the remaining
269 one tumor were withheld and used to test the model. Within each fold, the train set was balanced using Synthetic Minority
270 Oversampling Technique (SMOTE) to upsample the minority class to equal the majority class[38]. This process was repeated
271 until tissue regions from all 8 tumors appeared in the test set. Test set predictions were aggregated across the 8 folds into
272 one confusion matrix, and final performance metrics were calculated from this confusion matrix. Coefficients were recorded
273 for each of the 8 models and then averaged across all models to calculate final feature importance. Previously published
274 code[10] was used to perform the machine learning pipeline using Python software and the following packages: pandas,
275 numpy, scikit-learn, and imbalanced-learn. The elastic net classifier was built using scikit-learn's LogisticRegression
276 function with the 'penalty' and 'l1_ratio' parameters set to 'elasticnet' and 0.5, respectively.
277
278 *In vitro T cell activation and co-cultures*
279 Murine OT-I $CD8^+$ T cells were isolated from the spleens of OT-I transgenic mice (The Jackson Laboratory;
280 #003831) using the EasySep Mouse $CD8^+$ T cell Isolation Kit (Stemcell; 19853), which yielded an enrichment of 96%–
281 100% purity. Isolated $CD8^+$ T cells were stimulated *in vitro* with plate-bound anti-CD3 and anti-CD28 (5 µg/mL; BioXcell)
282 for 24 hours and expanded in RPMI-1640 (Gibco) completed with 10% FBS (Gibco), 1% nonessential amino acids (Gibco),
283 1% sodium pyruvate (Gibco), 1% penicillin/streptomycin (Gibco), 57 µmol/L 2-BME (Sigma), and 100 IU/mL of
284 recombinant human IL-2 (Peprotech).
285 For $CD8^+$ T cell co-culture with tumor cells, 50,000 $CD8^+$ T cells were incubated with 50,000 tumor cells in 96-
286 well round-bottom plates for 24 hours at 37°C with phorbol 12-myristate 13-acetate (PMA) (20 ng/mL, Sigma; P1585),
287 ionomycin (1 µg/mL, Sigma; I0634), and GolgiStop (BD; 554724). Intracellular staining was done using the
288 Fixation/Permeabilization Kit and antibodies used are listed in Supplementary Table 1. SIINFEKL tetramers were obtained
289 from the NIH tetramer core facility.
290
291 *RNA-sequencing*

292 RNA was isolated from frozen cells using RNeasy Mini Kit (Qiagen; 74106). RNA concentrations and quality were
293 assessed by NanoDrop spectrophotometer. Preparation of RNA library and transcriptome sequencing were conducted by
294 Novogene Co., Ltd using the HiSeq Illumina platform. Novogene analysis service aligned raw reads to GRCm38 genome
295 and performed DESeq2 differential expression analysis. Gene set enrichment analysis (GSEA) was done using GSEA v4.2.3
296 software with the MSigDB hallmark and curated gene sets[39,40].
297
298 *Ribonucleoprotein immunoprecipitation assay*
299 KPC cells were washed and harvested with cell scrapper in cold-PBS. Ribonucleoprotein immunoprecipitation
300 assay was done according to manufacturer's instructions (MilliporeSigma; 17-701) with modification to RNA purification.
301 Lysates were immunoprecipitated by using 10 μg of either anti-HuR antibody (Santa Cruz Biotechnology; sc-5261) or anti-
302 IgG control (MilliporeSigma; 12-371). For RNA purification from immunoprecipitation, the protocol was followed up to
303 the precipitation of RNA in ethanol, after which the entire mixture was transferred to an RNA column using the RNeasy
304 Micro Kit (Qiagen; 74004), and the manufacturer's instructions were followed thereafter. RNA quality was analyzed via
305 Bioanalyzer Pico chip by the Massively Parallel Sequencing Shared Resource Core at OHSU.
306 Preparation of RNA library and transcriptome sequencing were conducted by Novogene Co., Ltd using the HiSeq
307 Illumina platform. Novogene analysis service aligned raw reads to GRCm38 genome and performed HuR-enriched peak
308 annotation with MACS2 software[41]. KEGG (Kyoto Encyclopedia of Genes and Genomes) pathway enrichment analysis
309 was done on HuR-enriched peaks.
310
311 *Statistical analysis*
312 Data were analyzed using unpaired two-tailed Student's *t*-test and one-way ANOVA test. In all cases, two-tailed
313 tests with P values less than 0.05 were considered significant. Statistics were calculated using GraphPad Prism 10 software
314 (GraphPad Software Inc). Results were graphed as mean ± standard deviation for *in vitro* experiments and ± standard error
315 of mean for animal experiments. Experimental sample sizes were chosen using power calculations and preliminary
316 experiments. Samples that had undergone technical failure during processing were excluded from subsequent analysis.
317
318 *Data availability*

319 RNA-sequencing dataset is deposited at the GEO (Gene Expression Omnibus) database as GSE287307. RIP-
320 sequencing dataset is deposited as GSE287349.
321
322 **RESULTS**
323 *Tumor ELAVL1 (HuR) expression correlates with patient outcome and T cell infiltration in PDAC*
324 We previously demonstrated that the RNA-binding protein HuR is highly expressed and activated (i.e. translocated
325 to the cytoplasm) in PDAC compared to adjacent normal pancreas[24,42]. First, we applied a validated HuR activity signature
326 highlighting HuR-dependent transcripts[17] to a large RNA-sequencing dataset including surgical-resected PDAC patients[27],
327 and showed that a lower HuR target activity signature predicted significantly prolonged patient survival (**Fig. 1A**).
328 Separately, baseline immune infiltration has been demonstrated to be associated with overall prognosis and response to ICB
329 in a variety of cancers[43]. To further understand the relationship between HuR activity in PDAC and antitumor immune
330 activity, we assayed DISCO single-cell RNA sequencing datasets and found tumor-intrinsic HuR expression levels
331 negatively correlated with total $CD3^+$ lymphocyte infiltration, i.e., lower tumor-intrinsic *ELAVL1* mRNA levels were
332 associated with more abundant $CD3^+$ lymphocyte infiltration in patient samples (**Fig. 1B** and **C**). To determine the causative
333 relationship between tumor-intrinsic HuR and T cell infiltration, and antitumor function in PDAC, we used a syngenetic
334 implantable mouse model of PDAC (KPC)[25]. To first assess whether HuR activity is recapitulated in our KPC model as in
335 human PDAC, HuR protein expression and localization was visualized with IHC staining. In concordance with patient data,
336 the KPC tumors had higher expression of whole-cell HuR compared to the healthy mouse pancreas (**Fig. 1D** and **E**). These
337 findings support previous work that tumor-intrinsic HuR is a poor prognostic marker in PDAC and pro-oncogenic[17,44], and
338 in addition, negatively correlates with lymphocyte infiltration in PDAC. HuR is similarly elevated in the KPC model as in
339 human PDAC providing a strong rationale for the investigation of tumor-intrinsic HuR in this immunocompetent murine
340 PDAC model. To our knowledge, this is the first genetic assessment of the role of HuR in PDAC tumor *in vivo* in an immune
341 intact setting.
342
343 *Tumor-intrinsic HuR supports tumor growth in KPC model*
344 We first established KPC cells with CRISPR-Cas9 mediated *Elavl1* genetic deletion using electroporation of
345 scramble or *Elavl1* targeted sgRNAs complexed to purified recombinant Cas9 protein, as previously described[45]. We isolated
346 and expanded single cell clones from these KPC HuR knockout (KO) pooled cell lines and three clones with stable knockout

347 and proliferation performance were selected and used for subsequent analyses. We then validated and quantified CRISPR-
348 Cas9 mediated disruption of the *Elavl1* locus via insertion or deletion (INDEL) via Sanger sequencing for our isolated
349 clones (**Fig. 2A**). Accordingly, the clones had a significant reduction in HuR mRNA and lost HuR protein expression (**Fig.**
350 **2B** and **C**).

351 To determine the impact of HuR on PDAC progression *in vivo*, we subcutaneously implanted KPC cells subjected
352 to electroporation with scramble sgRNAs wildtype (WT) or sgRNAs targeting *Elavl1* (HuR-KO) into syngeneic C57BL/6
353 mice and tracked tumor growth over time. We found that the loss of tumor-intrinsic HuR significantly delayed growth over
354 time by area and by end point weight (**Fig. 2D** and **E**). However, Ki67 staining showed no difference in tumor cell
355 proliferation between these WT and HuR-KO tumors, suggesting that the decrease in tumor growth that resulted from the
356 loss of PDAC HuR was dependent on a tumor-host interaction (**Fig. 2F**). Importantly, re-expression of the *Elavl1* sequence
357 via durable retroviral transduction in these HuR-KO cells rescued the tumor growth defect (**Fig. 2F** and **G**). Cumulatively,
358 these data causatively demonstrate, in genetic gain and loss of function, that HuR is required for PDAC progression *in vivo*.
359

360 *HuR-dependent growth of PDAC is immune mediated in vivo*

361 Our compiled analysis of TCGA cohorts identified a negative correlation between *ELAVL1* mRNA abundance and
362 total lymphocytes infiltration, suggesting that tumor-intrinsic HuR may act to constrain local immune activity and promote
363 tumor progression. To define the functional relationship between endogenous antitumor immunity and tumor-intrinsic HuR,
364 we orthotopically implanted KPC WT or HuR-KO into the pancreas of C57BL/6 hosts. We again observed a significant
365 delay in growth in the HuR-KO tumors in comparison to KPC WT tumors in this physiological-relevant stromal and immune
366 microenvironment (**Fig. 3A**). To provide a more granular understanding of the endogenous immune response, we performed
367 enumerative and phenotypic assessment of intratumoral immune populations via flow cytometry. Our analysis revealed an
368 increase in the abundance of $CD4^+$ T cells in KPC HuR-KO tumors as compared to WT tumors (**Fig. 3B**). We also observed
369 an increase in $NK1.1^+$ T cells and $CD19^+$ B cells as a proportion of all $CD45^+$ leukocytes within HuR-KO tumors
370 (Supplementary Fig. S1A). Phenotypic analysis of the tumor-infiltrating T cells demonstrated that both $CD4^+$ and $CD8^+$ T
371 cells from HuR-KO tumors had a greater proportion expressing the transcription factor T-bet (*Tbx21*) (**Fig. 3C**). This is
372 consistent with ongoing T cell effector function and polarization towards T helper Type 1 (T_H1) effector specification, the
373 cell population responsible for antitumor activity[46]. Additionally, the percentage of $CD4^+$ $Foxp3^+$ regulatory T (T_{Reg}) cells
374 trended lower in HuR-KO tumors compared to WT tumors, although not statistically significant (Supplementary Fig. S1B).

375 Additionally, T cell surface activation phenotype markers CD25 and CD69 were more abundant on $CD4^+$ and $CD8^+$ T cells
376 from HuR-KO tumors than WT tumors, while cell cycle marker Ki-67 stayed the same between groups (**Fig. 3D**). Surface
377 expression of antigen presentation major histocompatibility complex (MHC) class I, H2-kb, and immune checkpoint protein,
378 PD-L1, on tumor cells was not significantly different between WT and HuR-KO tumors, suggesting HuR mediates immune
379 suppression in this model independently of antigen presentation or the expression of co-inhibitory surface ligands
380 (Supplementary Fig. S1C). However, PD-L1 level was significantly higher in total HuR-KO cells than WT cells, indicating
381 HuR-KO tumors were generally more immune activated (Supplementary Fig. S1D).

382 Lastly, to test the causal relationship between endogenous antitumor immunity and HuR-mediated tumor
383 progression, we performed antibody-mediated depletion of $CD4^+$ and $CD8^+$ T cells from C57BL/6 hosts followed by
384 orthotopic implantation of KPC tumors with or without HuR depletion. We found that depletion of $CD4^+$ and $CD8^+$ T cells
385 restored the tumor growth of HuR-KO tumors, suggesting that the defect in tumor growth of HuR-KO PDAC is due to a
386 comparative increase in endogenous T cell-mediated tumor control in the absence of tumor-intrinsic HuR (**Fig. 3A**).
387 Together these data indicate that the tumor regression in the KPC HuR-KO tumors is mediated by presence of activated T
388 cells, which are otherwise suppressed in WT conditions.

389

390 *HuR limits T cell infiltration and activation, promoting an immunosuppressive and myeloid-driven TME landscape*

391 Importantly, the TME is not just defined by the numerical presence of immune cells, but by how these cells are
392 spatially organized, enabling communication with one another. Contrary to flow cytometry, mIHC preserves the spatial
393 context of the tissue, providing deep phenotypic information and precise spatial locations of the cells present in the TME[26].
394 Prior research that utilized mIHC analysis has discovered novel cellular crosstalk and immunological niches that shape the
395 progression of PDAC[10,35]. Therefore, we investigate how HuR impacts the PDAC TME spatial landscape to identify the key
396 immunological crosstalk that led to HuR-mediated immune evasion. By performing mIHC on orthotopically implanted KPC
397 WT and HuR-KO tumors, 429,669 cells were assayed in total across 31 2.0 mm^2 tissue regions from 8 tumors (4 WT and 4
398 HuR-KO) by a 15-antibody mIHC panel (**Fig. 4A** and Supplementary Fig. S2A). Cells were hierarchically gated into 12
399 lineages, spanning lymphoid, myeloid, stromal, and neoplastic lineages (**Fig. 4B** and Supplemental Table 3). We then
400 quantified TME cellular composition and spatial architecture in three ways, as previously described[10]: (i) cell density, (ii)
401 cell–cell spatial proximities, and (iii) recurrent cellular neighborhoods (RCNs), resulting in 98 unique TME features
402 calculated per tissue region. Because of the quantity and complexity of the mIHC data, we leveraged the previously

403 published machine learning pipeline[10] to first train an elastic net model to classify tumor genotype (WT vs HuR-KO) of a
404 given tissue region based upon the 98 TME features, and then interrogate model coefficients as a means to perform feature
405 selection and unbiasedly identify the top underlying TME immunobiology distinguishing KPC WT tumors from HuR-KO
406 tumors.

407 Our machine learning model accurately classified tumor genotype (WT vs HuR-KO) as evidenced by an area under
408 the receiver operating characteristic curve (AUC) of 0.97, with additional performance metrics all scoring above 0.83 (**Fig.**
409 **4C** and Supplementary Fig. S2B). This high model performance enabled us to delve into the model coefficients representing
410 the weighted combination of top TME features differentiating WT versus HuR-KO tumors. Of the total 98 TME features,
411 the top 18 features discriminating WT tumors from HuR-KO tumors accounted for 80% of all coefficient weights driving
412 model predictions, and 15 of these top 18 features were statistically significant (**Fig. 4D** and Supplementary Fig. S2C);
413 together, these results indicate these features represent the majority of significant TME differences between WT and HuR-
414 KO tumors.

415 Consistent with our flow cytometry data (**Fig. 3A**), and despite the relatively low amount of T cells in the total cell
416 population, the model identified increased $CD4^+$ T cell density in the HuR-KO tumors as compared to the WT tumors (**Fig.**
417 **4B** and **D**). HuR-KO tumors also possessed increased densities of monocytes as compared to the WT tumors. Interestingly,
418 from a spatial perspective, the model detected an increase in cell–cell proximity (defined by 20μm in distance) between
419 $CD206^-$ macrophages and $CD4^+$ T cells in HuR-KO tumors, while WT tumors had an increase in spatial proximities
420 predominately involving neutrophils, $CD206^+$ macrophages and $CD11b^-$ macrophages, monocytes, and neoplastic
421 epithelium (**Fig. 4D** and Supplementary Fig. S2D). Delving deeper into these top spatial features highlighted by the model,
422 we found higher densities of Ki-67^+CD206^- macrophages (anti-tumoral "M1-like") and PD-1^+CD4^+ T cells in HuR-KO
423 tumors, which aligns with higher antitumor immunity in HuR-KO tumors (**Fig. 4E**). On the contrary, we found higher
424 densities of Ki-67^+neutrophils and PD-$L1^+$ $CD11b^-$ macrophages in WT tumors, which aligns with an immunosuppressive
425 phenotype in WT tumors (**Fig. 4F**).

426 The model also identified four RCNs as being main differentiators between WT and KO tumors. Briefly, RCNs
427 represent phenotypically distinct spatial groupings—or neighborhoods—of cells within a 60 μm radius of each other that
428 are present across tumor samples. Cells were clustered according to their neighborhood composition and were assigned to
429 one of eight RCNs, each with unique phenotypic compositions (**Fig. 4G**). The machine learning model identified that RCNs
430 3 and 6 (predominantly neoplastic epithelium and $CD11b^-$ macrophages) were enriched in KPC WT tumors, while RCNs 4

431 and 5 were enriched in HuR-KO tumors (**Fig 4D** and Supplemental Fig. S2E). RCN 4 had the most unique clustering of T
432 cells, CD206$^-$ macrophages, and monocytes (**Fig. 4G**), indicating a potential lymphoid-myeloid communication relationship
433 that supports T cell function in an HuR-dependent manner. Together, the mIHC results indicate that the TME phenotypic
434 and spatial landscape differs between HuR-deficient and HuR-competent PDAC tumors. Specifically, our results indicate
435 HuR mediates immune suppression by limiting T cell infiltration and activation, and instead promotes a myeloid-driven
436 immunosuppressive spatial landscape.
437
438 *HuR restricts the effector functions of CD4$^+$ and CD8$^+$ T cells in PDAC*
439 Drawing from our observation that tumor-intrinsic HuR suppressed the activation levels of PDAC-infiltrating T
440 cells, we next asked whether HuR constrained the acquisition of effector functions of tumor-infiltrating T cells. To that end,
441 we performed direct *ex vivo* reactivation of T cells infiltrating WT or HuR-KO PDAC tumors and captured and assessed
442 their cytokine production via intracellular cytokine staining quantified by flow cytometry. By unsupervised clustering all
443 CD4$^+$ T cells based on their cytokine production, CD4$^+$ T cells derived from WT and HuR-KO tumors naturally separated
444 in two clusters demonstrating their distinct phenotypes (**Fig. 5A**). Consistent with increase in activation markers, CD4$^+$ T
445 cells derived from HuR-KO tumors exhibited increase in cytokine production and polyfunctionality (**Fig. 5A** and **B**).
446 Additionally, CD8$^+$ T cell derived from HuR-KO tumors displayed an increase in IFN-γ production compared to CD8$^+$ T
447 cells derived from WT tumors (Supplementary Fig. S3A).
448
449 *HuR restricts the infiltration of antigen-specific CD4$^+$ and CD8$^+$ T cells in PDAC*
450 To determine the impact of HuR loss in PDAC on the function and abundance of tumor-specific T cells, we
451 retrovirally transduced KPC cells with an ovalbumin (OVA)-expressing construct to make KPC cells express full-length
452 OVA for processing and presentation on MHC (**Fig. 5D**, left). When *ex vivo* expanded and activated ovalbumin-specific
453 CD8$^+$ T cells (OT-I cells) were co-cultured with KPC OVA cells, we found that KPC WT OVA cells exhibited suppression
454 of OT-1 T cell cytokine production (IFN-γ and TNF-α production) relative to KPC HuR-KO OVA cells (**Fig. 5C**), despite
455 there being no difference in MHC-I abundance or antigen presentation in KPC HuR-KO cells in response to interferon
456 stimulation (**Fig. 5D**). This co-culture model continues to support the notion that tumor-intrinsic HuR suppresses local T
457 cell function in a manner independent of antigen presentation or interferon response. To evaluate the endogenous T cell
458 responses against the OVA antigen in the presence or absence of tumor-intrinsic HuR, HuR WT or HuR-KO OVA cells were

459 orthotopically implanted into C57BL/6 mice. Notably, KPC HuR-KO OVA tumors were rejected in 80% of mice, with
460 significantly smaller tumors than KPC WT OVA tumors in those instances where a tumor was indeed evident (**Fig. 5D**).
461 Given the absence of a pancreatic tumor in most instances of HuR-KO KPC OVA, we evaluated the peritumoral tissues in
462 both groups of tumor-bearing hosts. We found statistically significant increases in the amount of $CD8^+$ T cells, and OVA
463 tetramer$^+$ $CD8^+$ T cells in hosts bearing HuR-KO OVA tumors than WT OVA tumors (**Fig. 5E**). We observed much lower
464 SIINFEKL tetramer staining in the spleen of tumor bearing mice, and no difference in the amounts of OVA tetramer$^+$ $CD8^+$
465 T cells between spleens from WT tumor-bearing hosts compared to HuR-KO tumor-bearing hosts (**Fig. 5E**). Together these
466 data indicate that tumor-intrinsic HuR suppresses the number of functional populations (cytokine producing, and antigen-
467 specific) of T cells in the PDAC TME, thus promoting tumor immune evasion.
468
469 *HuR stabilizes anabolic transcripts and metabolic pathways*
470 To identify the mechanism underlying HuR-dependent immune suppression and tumor progression in our
471 immunocompetent model, we performed bulk-RNA sequencing on KPC WT and HuR-KO cells (Supplementary Fig. S4A).
472 GSEA analysis identified established signatures involved in MYC pathways and metabolic reprogramming, including
473 adipogenesis and cholesterol homeostasis, were higher in the KPC WT cells compared to the HuR-KO cells (Supplementary
474 Fig. S4A and B). Given that HuR is known to stabilize RNA by directly binding to the 3'UTR regions of transcripts, we
475 sought to identify those RNAs in the KPC WT cells using ribonucleoprotein immunoprecipitation (RIP) followed by high-
476 throughput RNA sequencing (**Fig. 6A**). We validated HuR-RIP pulldown with immunoblot analysis from the bead-bound
477 lysate and flow-through. Validating our protocol, motif analysis showed preferential binding to AU-rich sequences as
478 previously described for HuR (**Fig. 6C** and Supplementary Fig. S4C)[47]. Additionally, established HuR metabolism targets,
479 the *IDH1* 3' UTR[13], and the *Rictor* 3' UTR, demonstrated significantly peak enrichment in comparison to reference control
480 *GAPDH* loci (**Fig. 6B** and Supplementary Fig. S4D). KEGG pathway analysis of the 1847 bound mRNAs revealed
481 enrichment of transcripts involved in metabolism, including MAPK signaling, mTOR signaling, HIF1-α pathway and
482 proteoglycan pathways, consistent with a model wherein HuR drives PDAC nutrient consumption to the potential detriment
483 of adjacent cell populations (**Fig. 6D**).
484 To test our hypothesis that HuR increases mTOR activity and drives metabolic competition to suppress local T-cell
485 function, we pretreated KPC OVA cells with mTOR inhibitors (AZD8055 and Torin1) and IFN-γ, and then co-cultured the
486 pretreated KPC OVA cells with OVA-antigen specific OT-I cells (**Fig. 6E**). The pretreated KPC OVA cells had decreased

487 mTOR activity by the measurement of decreased levels of phosphorylated-ribosome subunit 6 (p-S6). Of note, we validated
488 that the inhibitors did not impair H2kb levels in these tumor cells (**Fig. 6F**). Confirming our hypothesis, we observed that
489 OT-I T cells co-cultured with mTOR-inhibited KPC WT OVA cells had increased cytokine production (IFN-γ and TNF) in
490 comparison to T cells co-cultured with vehicle-treated KPC WT OVA cells (**Fig. 6G** and **H**). In comparison, T cells co-
491 cultured with KPC HuR-KO OVA cells demonstrated higher cytokine production *de novo,* independent of additional mTOR
492 inhibition – suggesting overlap between the two pathways (**Fig. 6G** and **H**). This data further supports our hypothesis that
493 HuR-KO tumor cells have lower mTOR activity at baseline and as a result, less nutrient competition with T cells, thus
494 mTOR inhibition in HuR-KO tumor cells could not increase T cell function further. In addition, because of the different
495 inhibition capacity of different inhibitors, T cells co-cultured with tumor cells treated with mTOR1 and mTOR2 inhibitor,
496 Torin1, displayed increase in both IFN-γ and TNF production, while mTOR1 inhibitor, rapamycin, only displayed increase
497 in TNF production (**Fig. 6G** and **H**). Taken together, these data indicate mechanistically tumor-intrinsic HuR directly binds
498 to and stabilizes transcripts involved in mTOR pathways, and the HuR-mediated increase of mTOR activity in tumor
499 metabolic competes with local T cells and ultimately suppress T cell function.
500
501 *PDAC resistance to Immune checkpoint blockade is dependent on HuR*
502 As previous discussed, ICB showed limited response in PDAC patients with deficiency in DNA mismatch repair
503 machinery[7], which suggested that the PDAC TME is inherently immune suppressive. Drawing from the observation that
504 PDAC HuR is responsible for constraining the infiltration and function of tumor specific T cells, we next asked whether
505 PDAC therapeutic resistance to ICB treatment was dependent on HuR function. Following a published treatment regimen[3],
506 we treated KPC WT and HuR-KO tumors-bearing mice with αPD-1 or control αIgG (**Fig. 7A**). Consistent with prior reports,
507 αPD-1 treatment alone in KPC WT tumors did not lead to tumor regression. However, αPD-1 treatment in KPC HuR-KO
508 tumors induced significant and almost total tumor regression (**Fig. 7A**). The αPD-1 treatment did not induce significant loss
509 of body weight in mice, indicating the treatment was well-tolerated in both groups (**Fig. 7B**). Consistent with previous
510 observations (**Fig. 3A**), HuR depletion led to increased $CD4^+$ T cell infiltration in tumors. While αPD-1 treatment in HuR-
511 KO tumors did not further boost the $CD4^+$ T cell infiltration compared to the IgG treatment, interestingly, αPD-1 treatment
512 in HuR-KO tumors induced higher infiltration of $CD8^+$ T cells with no effect observed in the WT tumors (**Fig. 7C**). Together,
513 these data indicate that $CD8^+$ T cells are the main responder to αPD-1 treatment in HuR-KO tumors, and support our

514 hypothesis that HuR depletion in PDAC tumors provides a greater proportion of T cells in the TME, which increased the
515 capacity for enhanced antitumor effector activity.
516
517 **DISCUSSION**
518 The immune landscape of PDAC TME is highly immunosuppressive and is a major barrier to effective
519 immunotherapy response[2,8]. Hence, understanding the underlying molecular mechanisms is key to advancing
520 immunotherapy strategies. From multi-omics analysis on large patient databases, the RNA-binding protein, HuR, negatively
521 correlates with both patient survival and total lymphocytes infiltration in PDAC. Herein, we found that HuR expressed by
522 PDAC promotes tumor growth in the immunocompetent PDAC model. Within PDAC cells, HuR directly binds to and
523 stabilizes anabolic transcripts, ultimately limiting the abundance and function of $CD4^+$ and $CD8^+$ T cells. As the primary
524 mediators of antitumor immunity, the T cells in the HuR-proficient PDAC TME had limited effector functions in cytokine
525 production and antigen-specific response. This mechanism could be exploited with therapeutic potential, as depletion of
526 HuR sensitizes PDAC tumor to ICB treatment with increased efficacy.
527 In previous studies, loss of HuR in human PDAC xenografts in immunocompromised hosts had no impact on tumor
528 growth[24], which complements our findings that HuR has an immune-mediated tumor suppressive role. In addition, previous
529 work targeting overexpressing HuR in the mouse pancreas led to chronic inflammation in the TME and promoted tumor
530 development, indicating HuR contributes to an unbalanced inflamed environment[23]. Herein, this is the first report of PDAC
531 tumor-intrinsic HuR having a potent extrinsic effect on the immune cells in the TME. This new discovery of HuR function
532 fits with its known role in supporting tumor initial and tumor progression, and future study should investigate how HuR-
533 mediated immune suppression promotes PDAC initiation from pancreatitis. Similarly, another key transcriptional regulator
534 in PDAC, Myc, has been shown to control immune evasion in PDAC[11]. Therefore, studying pro-oncogenic molecules like
535 HuR and Myc in immune-competent models may provide a much-needed understanding of the post-transcriptional and
536 transcriptional tumor-intrinsic networks involved in immune suppression in the PDAC TME.
537 Interestingly, we did not observe a high correlation between gain/loss of RNA transcripts by RNA-sequencing and
538 alignment abundance on RNA-immunoprecipitation. Overlapping these HuR-bound targets with those whose expression
539 was reduced upon HuR-KO in the same cell lines identified 141 RNAs that are dependent on HuR binding to maintain
540 transcript levels (data not shown). While the low percentage of overlap was surprising, published works have observed
541 similar non-linear relationships between RNA-binding proteins and their targets[47,48]. These results further illustrate the

542 complicated regulation mechanisms of RNA-binding proteins with its binding targets in general. A more granular
543 understanding of the relationship between HuR 3' UTR binding and the impact on protein abundance will inform our ability
544 to leverage HuR function for translational purposes.

545 Transcriptomic analyses in our KPC model confirmed multiple dysregulated pathways, which have been previously
546 illustrated to be regulated by HuR[16,17]. Specifically, HuR directly upregulates multiple pathways in tumor remodeled
547 metabolism[13]. Metabolic reprogramming in the tumor through the Warburg effect, characterized by aerobic glycolysis, not
548 only enhances tumor proliferation but also depletes the limited resources within the TME[14,49]. Recent metabolite profiling
549 of the PDAC interstitial fluid showed altered nutrient availability and nutrient deprivation in the PDAC TME[50], suggesting
550 metabolic competition could be one of the mechanisms that tumor cells use to suppress immune cell function. Particularly,
551 reports have shown that activated T cells need to reprogram their glucose and lipid metabolism to support their effector
552 functions[51,52], and Tregs are more adapted to glucose deprivation with an increase in fatty-acid oxidation[53]. These required
553 nutrients are in concordance with the HuR-mediated dysregulated metabolic pathways, suggesting HuR mediates immune
554 suppression via metabolic competition in the PDAC TME. In lieu of this, previous finding that PDAC WT and HuR-KO
555 tumors grow similarly in immunocompromised model further supports the notion that HuR-mediated anabolic pathways do
556 not support tumor growth by proliferation[24], instead by inducing immune suppression. In total, our results warrant further
557 exploration to define the mechanistic connection between HuR-mediated PDAC metabolism and T cell function and
558 differentiation in the TME.

559 In the PDAC immune landscape, our findings once again demonstrate the potential of $CD8^+$ T cells to be harnessed
560 for PDAC tumor control, while also highlighting that $CD4^+$ T cells can play a crucial role in addition to well-described
561 $CD8^+$ T cells. Similar observations of $CD4^+$ T cells having anti-PDAC response were found in the setting of αCD40
562 stimulation[54]. These findings support the potential of targeting $CD4^+$ T cells to augment anti-tumor responses. In addition
563 to impacting T cells, our mIHC analysis demonstrated that tumor-intrinsic HuR may have a broader impact on the immune
564 landscape of the PDAC TME, impacting the spatial organization and proliferation status of multiple myeloid lineages,
565 including increased proliferation of neutrophils and decreased proliferation of anti-tumoral "M1-like" macrophages. PDAC-
566 infiltrating neutrophils have been implicated to associate with poor prognosis in patients[55,56], and our findings reveal a
567 potential novel upstream tumor-mediator regulator of neutrophil proliferation in PDAC. Still, the implications of these
568 findings highlight the need for further investigation into the mechanism of HuR mediated myeloid cell activities.

569 Broadly, these findings advance the paradigm that tumor-intrinsic mechanisms limit T cell infiltration and the
570 efficacy of anti-tumor immunity within the TME. Specifically, we highlight a novel role of tumor-intrinsic HuR as a
571 modulator of PDAC immune evasion. Currently, targeting strategies against HuR are under development (e.g., siHuR
572 nanotherapies and small molecule inhibitors)[57], and could potentially break PDAC resistance to immune-based anti-cancer
573 therapies (i.e., checkpoint blockade and T cell transfer) as demonstrated here in our pre-clinical KPC model. Because HuR
574 also has cell-intrinsic functions in intratumoral immune populations, further work will be required to understand the
575 combined impact of HuR inhibition on tumor control.
576

577 **FIGURE LEGENDS**

578 **Figure 1. Tumor ELAVL1 (HuR) expression correlates with patient outcome and T cell infiltration in PDAC**

579 **(A)** Kaplan-Meier plots demonstrating proportional overall survival in PDAC patients (n = 199) distinguished by low versus
580 high HuR Activity Signature.

581 **(B)** Scatter plot showing the Spearman's correlation between ELAVL1 expression in tumor cells and lymphocyte infiltration,
582 including CD8+ T cells, CD4+ T cells, and NK cells (n = 115 patients) and **(C)** violin plot demonstrating the difference in
583 lymphocyte infiltration in HuR- low and HuR-high tumors from the same samples.

584 **(D)** Representative images from patient tumor microarrays and KPC tumors stained for HuR expression and **(E)**
585 quantification of HuR protein staining intensity of normal pancreas, KPC GEMM (n=3) and xenograft tumors (n = 8).
586 Error bars represent standard error of the mean. ns, not significant; **P < 0.01; ***P < 0.005; ****P < 0.001, unpaired 2-
587 tailed Student's t tests **(C,E)**.
588

589 **Figure 2. Tumor-intrinsic HuR supports tumor growth in KPC model**

590 (**A**) INDEL quantification of single-cell clones isolated from CRISPR-Cas9 mediated disruption of the *Elavl1* locus in
591 KPC8069 tumor cells and (**B**) quantification of mRNA abundance by RT-qPCR and (**C**) protein abundance by immunoblot
592 of the same clones.

593 (**D**) Rates of subcutaneous KPC tumor growth represented over time following implant of KPC WT and HuR-KO tumor
594 cells (n = 5). (**E**) Summary quantification and pictures of the final tumor weight and size on day 34.

595 (**F**) Quantification of the percentages of $Ki67^+$ cells in total non-immune cells in subcutaneous KPC tumors by flow
596 cytometry (n = 5).

597 (**G**) Histogram and quantification of flow cytometry analysis of HuR expression in KPC WT and HuR-KO tumor cells
598 retrovirally transduced with empty vector or HuR-overexpression vector prior to subcutaneous implantation to C57BL/6
599 hosts (n = 10). (**H**) Summary quantification of the final tumor weight on day 30.
600 Error bars represent standard deviation (**B,F**) and standard error of the mean (**D,E,F,G,H**). *P < 0.05; **P < 0.01; ****P <
601 0.001, one-way ANOVA test (**B,G,H**), unpaired 2-tailed Student's t tests (**D,E,F**).
602
603 **Figure 3**. **HuR-dependent growth of PDAC is immune mediated *in vivo***
604 (**A**) Representative flow cytometry illustrating enumerating T cells in host spleens treated with IgG or αCD4/8 before and
605 during orthotopic tumor implantation and summary analysis of final KPC WT and HuR-KO tumor weight in host with or
606 without T cell depletion (n = 6) .
607 (**B**) Summary analysis enumerating tumor infiltrating lymphocytes (TIL) in orthotopic KPC WT and HuR-KO tumors (n =
608 5).
609 (**C**) Summary data depicting CD4 and CD8 T-cell Tbet^{+} percentages and (**D**) representative flow cytometry plot and
610 summary data depicting CD25 and CD69 phenotypic states on CD4 and CD8 T cells as in (**B**).
611 Error bars represent standard error of the mean. *P < 0.05; **P < 0.01; ***P < 0.005; ****P < 0.001, one-way ANOVA test
612 (**A**), unpaired 2-tailed Student's t tests (**B,C,D**).
613
614 **Figure 4**. **HuR limits T cell infiltration and activation, promoting an immunosuppressive and myeloid-driven TME**
615 **landscape**
616 (**A**) Representative pseudo-colored mIHC images showing CD206, F4/80 (macrophages), and CD3 (T cells) in KPC WT
617 tumors (left) and in HuR-KO tumors (right) and (**B**) summary data depicting averaged immune cell density in KPC WT
618 (n=4) and HuR-KO tumors (n = 4).
619 (**C**) ROC curve with corresponding AUC for the machine learning model.
620 (**D**) Model coefficients for the top 18 features that drove the machine learning model to predict tumor genotype WT (black)
621 or HuR-KO (blue). Features are ranked by importance of TME feature type to distinguish tumor genotype.
622 (**E**) Summary data depicting densities of Ki67^{+}CD206^{-} macrophages and PD1^{+}CD4^{+} T cells and (**F**) summary data depicting
623 densities of Ki67^{+}neutrophils and PD-L1^{+} CD11b^{-} macrophages in KPC WT (n= 20 tissue regions) and HuR-KO tumors (n
624 = 11 tissue regions).

625 (**G**) Stacked bar chart showing the average cellular composition of each of eight RCNs.

626 Error bars represent standard error of the mean. *P < 0.05; **P < 0.01; ***P < 0.005; ****P < 0.001, Mann–Whitney U-

627 test to determine statistical significance (**E,F**).

628

629 **<u>Figure 5</u>. HuR restricts the function and infiltration CD4 and CD8 T cells in PDAC**

630 (**A**) Concatenated single-cell overlay and colorimetric density tSNE based depiction of the indicated proteins by flow

631 cytometry, and (**B**) representative and summary quantification of cytokines following *ex vivo* stimulation of isolated $CD4^+$

632 T cells from KPC WT and HuR-KO tumors (n = 5).

633 (**C**) Representative flow cytometry plot and summary data depicting cytokine productions of OT-I $CD8^+$ T cells co-cultured

634 with KPC WT OVA or KPC HuR-KO OVA tumor cells (n = 3).

635 (**D**) Representative flow cytometry plot depicting HuR expression and Kb-SIIN staining of KPC WT OVA or KPC HuR-

636 KO OVA tumor cells prior to orthotopic implantation, and summary data of tumor rejection rate and final tumor weight at

637 day 20. (**E**) Representative flow cytometry plot and summary data enumerating spleen and pancreas infiltrating $CD8^+$ T

638 cells and $SIIN^+$ $CD8^+$ T cells from KPC WT OVA and KPC HuR-KO OVA tumor-bearing mice (n = 5).

639 Error bars represent stand deviation (**C**) and standard error of the mean (**B,D,E**). *P < 0.05; **P < 0.01; ***P < 0.005; ****P

640 < 0.001, unpaired 2-tailed Student's t tests.

641

642 **<u>Figure 6</u>. HuR stabilizes anabolic transcripts and metabolic pathways**

643 (**A**) Schematic depicting RIP-seq process to identify HuR-bound transcript (n = 3). (**B**) RIP-seq reads genome alignment

644 plot to *IDH1 and Rictor* loci (3'UTR region highlighted with red box). (**C**) Representative immunoblot validation of HuR

645 pulldown in KPC cells in comparison to IgG control. (**D**) Summary depiction of enrichment scores (RichFactor) of KEGG

646 pathways with transcripts comparatively enriched in HuR-IP samples.

647 (**E**) Schematic depicting the pre-treatment of tumor cells with mTOR inhibitors (Rapamycin and Torin1) and IFN-γ before

648 co-culture with OT-I T cells. (**F**) Representative flow cytometry plot depicting *p*-S6 and H2-Kb staining of KPC WT OVA

649 cells after mTOR inhibitors and IFN-γ treatments. (**G**, **H**) Summary data depicting cytokine productions of OT-I $CD8^+$ T

650 cells co-cultured with pre-treated KPC WT OVA or KPC HuR-KO OVA tumor cells (n = 3).

651 Error bars represent stand deviation (**G**, **H**). *P < 0.05; ***P < 0.005; ****P < 0.001, one-way ANOVA test.

652

653 **<u>Figure 7</u>. PDAC resistance to immune checkpoint blockade is dependent on HuR**

654 (**A**) Schematic for αPD-1 treatment on KPC tumor bearing mice, and summary data on final tumor weight at day15. (**B**)
655 Body weight of mice in (**A**) by group tracked over time (n = 4).

656 (**C**) Summary analysis enumerating tumor infiltrating lymphocytes (TIL) of KPC WT and HuR-KO tumors in mice received
657 IgG or αPD-1 treatment in (**A**).

658 Error bars represent standard error of the mean. *P < 0.05; **P < 0.01, unpaired 2-tailed Student's t tests (**A**), one-way
659 ANOVA test (**C**).

660

661 **<u>Supplement Figure 1</u>. Tumor-intrinsic HuR mediates immune composition in the PDAC TME.**

662 (**A**) Summary analysis enumerating tumor infiltrating NK cells, B cells, dendritic cells, macrophages, and (**B**) $Foxp3^+$ CD4
663 T-cell percentages.

664 (**C**) Summary data depicting H2-kb and PD-L1 expression on non-immune cells, and (**D**) PD-L1 expression on all cells in
665 orthotopic KPC WT and HuR-KO tumors (n = 5).

666 Error bars represent standard error of the mean. *P < 0.05; ***P < 0.005, unpaired 2-tailed Student's t tests.

667

668 **<u>Supplement Figure 2</u>. HuR limits T cell infiltration and activation, promoting an immunosuppressive and myeloid-**
669 **driven TME landscape**

670 (**A**) Summary data depicting average stromal, immune, and neoplastic epithelium cell density in KPC WT (n=4) and HuR-
671 KO tumors (n = 4).

672 (**B**) Bar chart showing performance metrics for the machine learning model. (**C**) Violin plot showing the normalized values
673 of the top 18 features driving the model. Features are organized by type on y-axis and $\log_{10+1}$ normalized values are shown
674 on the x-axis.

675 (**D**) Heatmaps showing average normalized frequency of spatial proximities between two cell types for each tumor group.

676 (**E**) Summary data showing average fraction of RCNs present in KPC WT (n=4) and HuR-KO (n=4) tumors and scatterplot
677 reconstructions of representative tissue regions with each cell colored by its RCN designation.

678 Error bars represent standard error of the mean. *P < 0.05, Mann–Whitney U-test to determine statistical significance (**C**).

679

680 **<u>Supplement Figure 3</u>. HuR restricts the function and infiltration CD4 and CD8 T cells in PDAC**

681 (**A**) Summary quantification of IFN-γ production following *ex vivo* stimulation of isolated CD8+ T cells from KPC WT and

682 HuR-KO tumors (n = 5).

683 Error bars represent standard error of the mean. **P < 0.01, unpaired 2-tailed Student's t tests.

684

685 **Supplement Figure 4**. **HuR stabilizes anabolic transcripts and metabolic pathways**

686 (**A**) Schematic and volcano plot depicting whole-transcriptomic changes between KPC WT and KPC HuR-KO tumor cells

687 (n = 3). (**B**) Summary depiction of normalized enrichment scores (NES) of gene-sets with transcripts comparatively enriched

688 or lost between indicated groups.

689 (**C**) Top 2 motif enrichment sequences from HuR-IP targets. (**D**) RIP-seq reads genome alignment plot to *GAPDH* locus

690 (3'UTR region highlighted with red box).

691 FDR q-value < 0.05, weighted Kolmogorov–Smirnov statistic test (**B**).

692

693 **Supplement Table 1**. **Antibody information for flow cytometry staining**

694 **Supplement Table 2**. **Antibody information for mIHC staining**

695 **Supplement Table 3**. **Gating strategies for lineage assignment in mIHC**

696

697 **REFERENCES**

698 1. Siegel RL, Miller KD, Wagle NS, Jemal A. Cancer statistics, 2023. *CA Cancer J Clin*. 2023;73(1):17-48.
699 doi:10.3322/caac.21763

700 2. Polani F, Grierson PM, Lim KH. Stroma-targeting strategies in pancreatic cancer: Past lessons, challenges and
701 prospects. *World J Gastroenterol*. 2021;27(18):2105-2121. doi:10.3748/wjg.v27.i18.2105

702 3. Evans RA, Diamond MS, Rech AJ, et al. Lack of immunoediting in murine pancreatic cancer reversed with neoantigen.
703 *JCI Insight*. 2016;1(14). doi:10.1172/jci.insight.88328

704 4. Freed-Pastor WA, Lambert LJ, Ely ZA, et al. The CD155/TIGIT axis promotes and maintains immune evasion in
705 neoantigen-expressing pancreatic cancer. *Cancer Cell*. 2021;39(10):1342-1360.e14. doi:10.1016/j.ccell.2021.07.007

706 5. Bailey P, Chang DK, Forget MA, et al. Exploiting the neoantigen landscape for immunotherapy of pancreatic ductal
707 adenocarcinoma. *Sci Rep*. 2016;6(1):35848. doi:10.1038/srep35848

708 6. Concha-Benavente F, Srivastava R, Ferrone S, Ferris RL. Immunological and clinical significance of HLA class I
709 antigen processing machinery component defects in malignant cells. *Oral Oncol*. 2016;58:52-58.
710 doi:10.1016/j.oraloncology.2016.05.008

711 7. Marabelle A, Le DT, Ascierto PA, et al. Efficacy of Pembrolizumab in Patients With Noncolorectal High Microsatellite
712 Instability/Mismatch Repair–Deficient Cancer: Results From the Phase II KEYNOTE-158 Study. *J Clin Oncol*.
713 2020;38(1):1-10. doi:10.1200/JCO.19.02105

714 8. Ino Y, Yamazaki-Itoh R, Shimada K, et al. Immune cell infiltration as an indicator of the immune microenvironment of
715 pancreatic cancer. *Br J Cancer*. 2013;108(4):914-923. doi:10.1038/bjc.2013.32

716 9. Gu H, Deng W, Zheng Z, Wu K, Sun F. CCL2 produced by pancreatic ductal adenocarcinoma is essential for the
717 accumulation and activation of monocytic myeloid-derived suppressor cells. *Immun Inflamm Dis*. 2021;9(4):1686-
718 1695. doi:10.1002/iid3.523

719 10. Blise KE, Sivagnanam S, Betts CB, et al. Machine Learning Links T-cell Function and Spatial Localization to
720 Neoadjuvant Immunotherapy and Clinical Outcome in Pancreatic Cancer. *Cancer Immunol Res*. 2024;12(5):544-558.
721 doi:10.1158/2326-6066.CIR-23-0873

722 11. Krenz B, Gebhardt-Wolf A, Ade CP, et al. MYC- and MIZ1-Dependent Vesicular Transport of Double-Strand
723 RNA Controls Immune Evasion in Pancreatic Ductal Adenocarcinoma. *Cancer Res*. 2021;81(16):4242-4256.
724 doi:10.1158/0008-5472.CAN-21-1677

725 12. Blanco FF, Jimbo M, Wulfkuhle J, et al. The mRNA-binding protein HuR promotes hypoxia-induced
726 chemoresistance through posttranscriptional regulation of the proto-oncogene PIM1 in pancreatic cancer cells.
727 *Oncogene*. 2016;35(19):2529-2541. doi:10.1038/onc.2015.325

728 13. Zarei M, Lal S, Parker SJ, et al. Posttranscriptional Upregulation of IDH1 by HuR Establishes a Powerful
729 Survival Phenotype in Pancreatic Cancer Cells. *Cancer Res*. 2017;77(16):4460-4471. doi:10.1158/0008-5472.CAN-17-
730 0015

731 14. Chang CH, Qiu J, O'Sullivan D, et al. Metabolic Competition in the Tumor Microenvironment Is a Driver of
732 Cancer Progression. *Cell*. 2015;162(6):1229-1241. doi:10.1016/j.cell.2015.08.016

733 15. Li W, Pan X, Chen L, et al. Cell metabolism-based optimization strategy of CAR-T cell function in cancer
734 therapy. *Front Immunol*. 2023;14. doi:10.3389/fimmu.2023.1186383

735 16. Lal S, Burkhart RA, Beeharry N, et al. HuR post-transcriptionally regulates WEE1: Implications for the DNA
736 damage response in pancreatic cancer cells. *Cancer Res*. 2014;74(4):1128-1140. doi:10.1158/0008-5472.CAN-13-1915

737 17. Brown SZ, McCarthy GA, Carroll JR, et al. The RNA-Binding Protein HuR Posttranscriptionally Regulates the
738 Protumorigenic Activator YAP1 in Pancreatic Ductal Adenocarcinoma. *Mol Cell Biol*. 2022;42(7):e00018-22.
739 doi:10.1128/mcb.00018-22

740 18. Kim HH, Yang X, Kuwano Y, Gorospe M. Modification at HuR(S242) Alters HuR Localization and Proliferative
741 Influence. *Cell Cycle Georget Tex*. 2008;7(21):3371-3377.

742 19. Anand S, Khan MA, Zubair H, et al. MYB sustains hypoxic survival of pancreatic cancer cells by facilitating
743 metabolic reprogramming. *EMBO Rep*. 2023;24(3):e55643. doi:10.15252/embr.202255643

744 20. Huang F, Bu L, Li M, et al. HuR/miR-124-3p/VDR complex bridges lipid metabolism and tumor development in
745 colorectal cancer. *Carcinogenesis*. 2025;46(1):bgae061. doi:10.1093/carcin/bgae061

746 21. Osma-Garcia IC, Capitan-Sobrino D, Mouysset M, et al. The RNA-binding protein HuR is required for
747 maintenance of the germinal centre response. *Nat Commun*. 2021;12(1):6556. doi:10.1038/s41467-021-26908-2

748 22. Shao Z, Tu Z, Shi Y, et al. RNA-Binding Protein HuR Suppresses Inflammation and Promotes Extracellular
749 Matrix Homeostasis via NKRF in Intervertebral Disc Degeneration. *Front Cell Dev Biol*. 2020;8:611234.
750 doi:10.3389/fcell.2020.611234

751 23. Peng W, Furuuchi N, Aslanukova L, et al. Elevated HuR in Pancreas Promotes a Pancreatitis-Like Inflammatory
752 Microenvironment That Facilitates Tumor Development. *Mol Cell Biol*. 2018;38(3):e00427-17.
753 doi:10.1128/MCB.00427-17

24. McCarthy GA, Di Niro R, Finan JM, et al. Deletion of the mRNA stability factor ELAVL1 (HuR) in pancreatic cancer cells disrupts the tumor microenvironment integrity. *NAR Cancer*. 2023;5(2):zcad016. doi:10.1093/narcan/zcad016

25. Hingorani SR, Wang L, Multani AS, et al. Trp53R172H and KrasG12D cooperate to promote chromosomal instability and widely metastatic pancreatic ductal adenocarcinoma in mice. *Cancer Cell*. 2005;7(5):469-483. doi:10.1016/j.ccr.2005.04.023

26. Tsujikawa T, Kumar S, Borkar RN, et al. Quantitative Multiplex Immunohistochemistry Reveals Myeloid-Inflamed Tumor-Immune Complexity Associated with Poor Prognosis. *Cell Rep*. 2017;19(1):203-217. doi:10.1016/j.celrep.2017.03.037

27. Link JM, Eng JR, Pelz C, et al. Ongoing replication stress tolerance and clonal T cell responses distinguish liver and lung recurrence and outcomes in pancreatic cancer. *Nat Cancer*. 2025;6(1):123-144. doi:10.1038/s43018-024-00881-3

28. Soneson C, Love MI, Robinson MD. Differential analyses for RNA-seq: transcript-level estimates improve gene-level inferences. *F1000Research*. 2016;4:1521. doi:10.12688/f1000research.7563.2

29. Love MI, Huber W, Anders S. Moderated estimation of fold change and dispersion for RNA-seq data with DESeq2. *Genome Biol*. 2014;15(12):550. doi:10.1186/s13059-014-0550-8

30. Hänzelmann S, Castelo R, Guinney J. GSVA: gene set variation analysis for microarray and RNA-Seq data. *BMC Bioinformatics*. 2013;14(1):7. doi:10.1186/1471-2105-14-7

31. Therneau T (2022). A Package for Survival Analysis in R. R package version 3.3-1, https://CRAN.R-775 project.org/package=survival.

32. Kassambara A, Kosinski M, and Biecek P (2021). survminer: Drawing Survival Curves using 'ggplot2'. R 777 package version 0.4.9. https://CRAN.R-project.org/package=survminer

33. Li M, Zhang X, Ang KS, et al. DISCO: a database of Deeply Integrated human Single-Cell Omics data. *Nucleic Acids Res*. 2022;50(D1):D596-D602. doi:10.1093/nar/gkab1020

34. Nofech-Mozes I, Soave D, Awadalla P, Abelson S. Pan-cancer classification of single cells in the tumour microenvironment. *Nat Commun*. 2023;14(1):1615. doi:10.1038/s41467-023-37353-8

35. Liudahl SM, Betts CB, Sivagnanam S, et al. Leukocyte Heterogeneity in Pancreatic Ductal Adenocarcinoma: Phenotypic and Spatial Features Associated with Clinical Outcome. *Cancer Discov*. 2021;11(8):2014-2031. doi:10.1158/2159-8290.CD-20-0841

36. Sivagnanam S, Betts C, Coussens LM 2023. Multiplex IHC Image Processing V0.2. protocols.io, 786 https://dx.doi.org/10.17504/protocols.io.n92ldmmznl5b/v2

37. Carpenter AE, Jones TR, Lamprecht MR, et al. CellProfiler: image analysis software for identifying and quantifying cell phenotypes. *Genome Biol*. 2006;7(10):R100. doi:10.1186/gb-2006-7-10-r100

38. Chawla NV, Bowyer KW, Hall LO, Kegelmeyer WP. SMOTE: Synthetic Minority Over-sampling Technique. *J Artif Intell Res*. 2002;16:321-357. doi:10.1613/jair.953

39. Subramanian A, Tamayo P, Mootha VK, et al. Gene set enrichment analysis: a knowledge-based approach for interpreting genome-wide expression profiles. *Proc Natl Acad Sci U S A*. 2005;102(43):15545-15550. doi:10.1073/pnas.0506580102

40. Liberzon A, Birger C, Thorvaldsdóttir H, Ghandi M, Mesirov JP, Tamayo P. The Molecular Signatures Database (MSigDB) hallmark gene set collection. *Cell Syst*. 2015;1(6):417-425. doi:10.1016/j.cels.2015.12.004

794 41. Zhang Y, Liu T, Meyer CA, et al. Model-based Analysis of ChIP-Seq (MACS). *Genome Biol*. 2008;9(9):R137.
795 doi:10.1186/gb-2008-9-9-r137

796 42. Lal S, Cheung EC, Zarei M, et al. CRISPR Knockout of the HuR Gene Causes a Xenograft Lethal Phenotype.
797 *Mol Cancer Res*. 2017;15(6):696-707. doi:10.1158/1541-7786.MCR-16-0361

798 43. Carstens JL, Correa de Sampaio P, Yang D, et al. Spatial computation of intratumoral T cells correlates with
799 survival of patients with pancreatic cancer. *Nat Commun*. 2017;8(1):15095. doi:10.1038/ncomms15095

800 44. Richards NG, Rittenhouse DW, Freydin B, et al. HuR Status is a Powerful Marker for Prognosis and Response to
801 Gemcitabine-Based Chemotherapy for Resected Pancreatic Ductal Adenocarcinoma Patients. *Ann Surg*.
802 2010;252(3):499. doi:10.1097/SLA.0b013e3181f1fd44

803 45. Collier C, Wucherer K, McWhorter M, et al. Intracellular K+ Limits T-cell Exhaustion and Preserves Antitumor
804 Function. *Cancer Immunol Res*. 2024;12(1):36-47. doi:10.1158/2326-6066.CIR-23-0319

805 46. Fridman WH, Pagès F, Sautès-Fridman C, Galon J. The immune contexture in human tumours: impact on clinical
806 outcome. *Nat Rev Cancer*. 2012;12(4):298-306. doi:10.1038/nrc3245

807 47. Rothamel K, Arcos S, Kim B, et al. ELAVL1 primarily couples mRNA stability with the 3′ UTRs of interferon-
808 stimulated genes. *Cell Rep*. 2021;35(8):109178. doi:10.1016/j.celrep.2021.109178

809 48. Antal CE, Oh TG, Aigner S, et al. A super-enhancer-regulated RNA-binding protein cascade drives pancreatic
810 cancer. *Nat Commun*. 2023;14(1):5195. doi:10.1038/s41467-023-40798-6

811 49. Hanahan D, Weinberg RA. Hallmarks of Cancer: The Next Generation. *Cell*. 2011;144(5):646-674.
812 doi:10.1016/j.cell.2011.02.013

813 50. Sullivan MR, Danai LV, Lewis CA, et al. Quantification of microenvironmental metabolites in murine cancers
814 reveals determinants of tumor nutrient availability. DeBerardinis R, van Lohuizen M, DeBerardinis R, Frezza C, eds.
815 *eLife*. 2019;8:e44235. doi:10.7554/eLife.44235

816 51. Kidani Y, Elsaesser H, Hock MB, et al. Sterol regulatory element–binding proteins are essential for the metabolic
817 programming of effector T cells and adaptive immunity. *Nat Immunol*. 2013;14(5):489-499. doi:10.1038/ni.2570

818 52. Leone RD, Powell JD. Metabolism of immune cells in cancer. *Nat Rev Cancer*. 2020;20(9):516-531.
819 doi:10.1038/s41568-020-0273-y

820 53. Yan Y, Huang L, Liu Y, et al. Metabolic profiles of regulatory T cells and their adaptations to the tumor
821 microenvironment: implications for antitumor immunity. *J Hematol OncolJ Hematol Oncol*. 2022;15:104.
822 doi:10.1186/s13045-022-01322-3

823 54. Morrison AH, Diamond MS, Hay CA, Byrne KT, Vonderheide RH. Sufficiency of CD40 activation and immune
824 checkpoint blockade for T cell priming and tumor immunity. *Proc Natl Acad Sci U S A*. 2020;117(14):8022-8031.
825 doi:10.1073/pnas.1918971117

826 55. Jin L, Kim HS, Shi J. Neutrophil in the Pancreatic Tumor Microenvironment. *Biomolecules*. 2021;11(8):1170.
827 doi:10.3390/biom11081170

828 56. Nielsen SR, Strøbech JE, Horton ER, et al. Suppression of tumor-associated neutrophils by lorlatinib attenuates
829 pancreatic cancer growth and improves treatment with immune checkpoint blockade. *Nat Commun*. 2021;12(1):3414.
830 doi:10.1038/s41467-021-23731-7

831 57. Finan JM, Sutton TL, Dixon DA, Brody JR. Targeting the RNA-Binding Protein HuR in Cancer. *Cancer Res*.
832 2023;83(21):3507-3516. doi:10.1158/0008-5472.CAN-23-0972

833

Figure 1

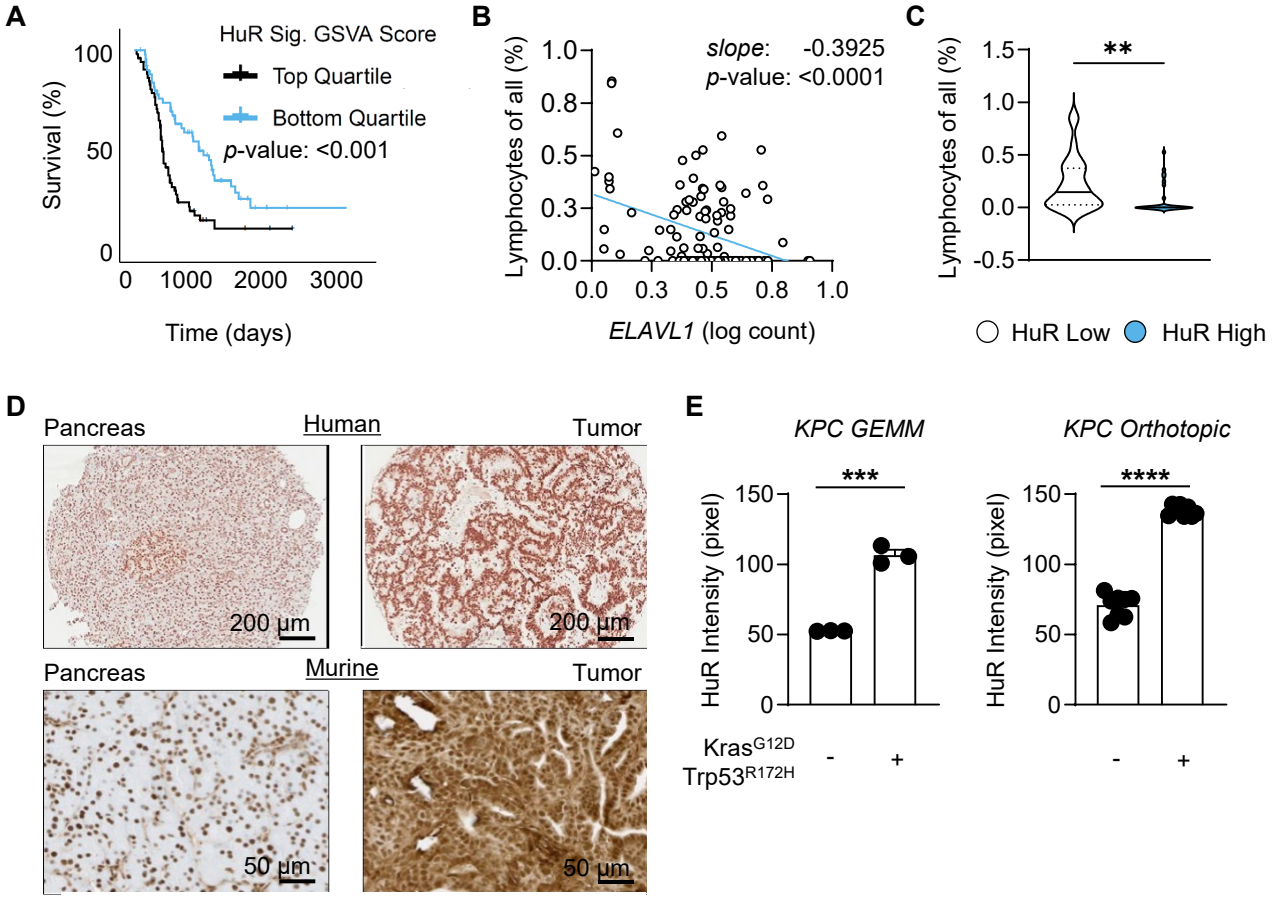

<u>Figure 1.</u> Tumor ELAVL1 (HuR) expression correlates with patient outcome and T cell infiltration in PDAC

(A) Kaplan-Meier plots demonstrating proportional overall survival in PDAC patients (n = 199) distinguished by low versus high HuR Activity Signature.

(B) Scatter plot showing the Spearman's correlation between ELAVL1 expression in tumor cells and lymphocyte infiltration, including CD8+ T cells, CD4+ T cells, and NK cells (n = 115 patients) and **(C)** violin plot demonstrating the difference in lymphocyte infiltration in HuR- low and HuR-high tumors from the same samples.

(D) Representative images from patient tumor microarrays and KPC tumors stained for HuR expression and **(E)** quantification of HuR protein staining intensity of normal pancreas, KPC GEMM (n=3) and xenograft tumors (n = 8).

Error bars represent standard error of the mean. ns, not significant; **P < 0.01; ***P < 0.005; ****P < 0.001, unpaired 2-tailed Student's t tests **(C,E)**.

Figure 2

A

Clone	ICE	KO-Score	R^2	Indels
KO6	80	74	0.8	{'1': 7.0, '-1': 67.0, '-3': 6.0}
KO8	97	97	0.97	{'-1': 97.0}
KO9	93	93	0.93	{'-1': 83.0, '-2': 10.0}

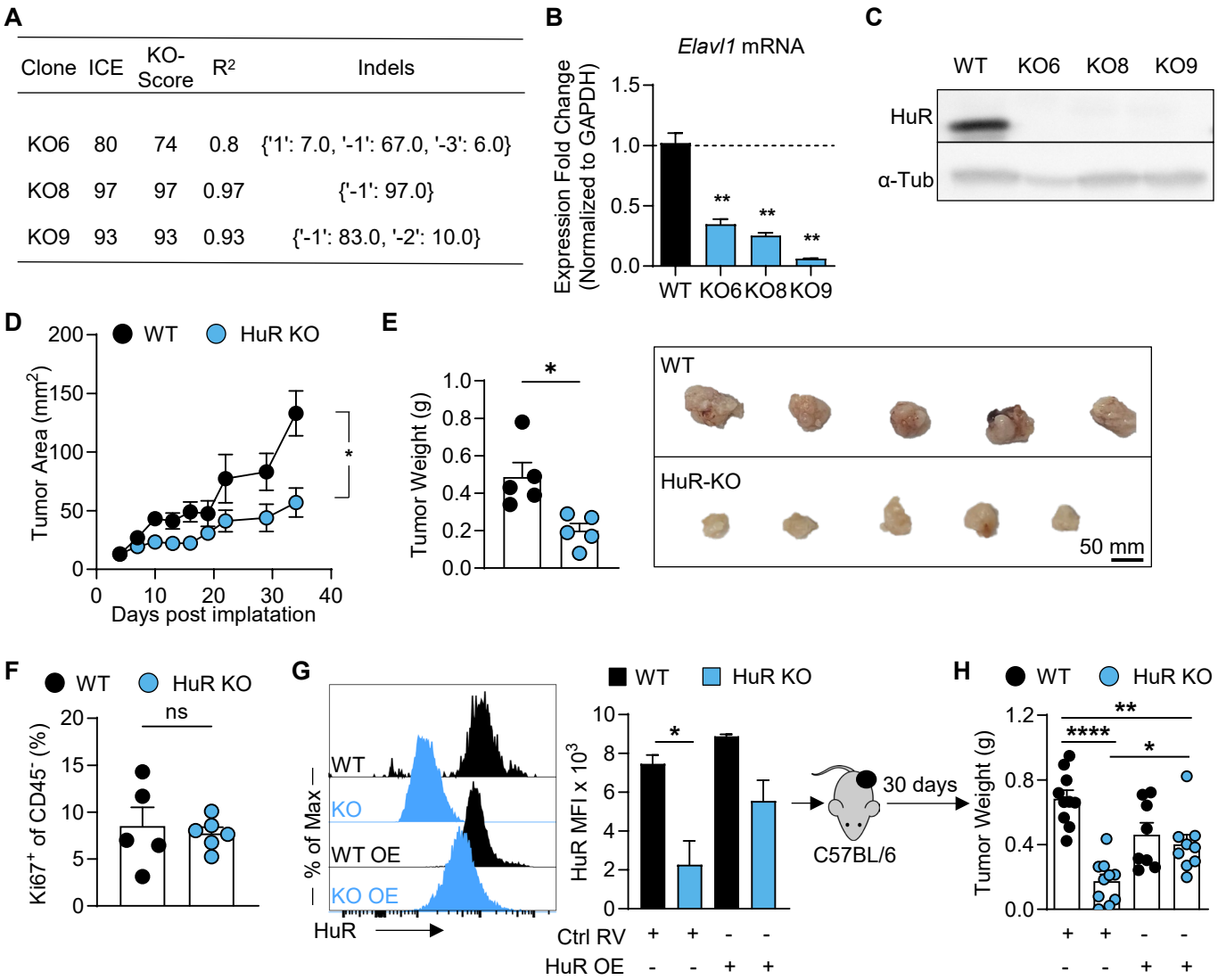

Figure 2. **Tumor-intrinsic HuR supports tumor growth in KPC model**

(**A**) INDEL quantification of single-cell clones isolated from CRISPR-Cas9 mediated disruption of the *Elavl1* locus in KPC8069 tumor cells and (**B**) quantification of mRNA abundance by RT-qPCR and (**C**) protein abundance by immunoblot of the same clones.

(**D**) Rates of subcutaneous KPC tumor growth represented over time following implant of KPC WT and HuR-KO tumor cells (n = 5). (**E**) Summary quantification and pictures of the final tumor weight and size on day 34.

(**F**) Quantification of the percentages of $Ki67^+$ cells in total non-immune cells in subcutaneous KPC tumors by flow cytometry (n = 5).

(**G**) Histogram and quantification of flow cytometry analysis of HuR expression in KPC WT and HuR-KO tumor cells retrovirally transduced with empty vector or HuR-overexpression vector prior to subcutaneous implantation to C57BL/6 hosts (n = 10). (**H**) Summary quantification of the final tumor weight on day 30.

Error bars represent standard deviation (**B,F**) and standard error of the mean (**D,E,F,G,H**). *P < 0.05; **P < 0.01; ****P < 0.001, one-way ANOVA test (**B,G,H**), unpaired 2-tailed Student's t tests (**D,E,F**).

Figure 3

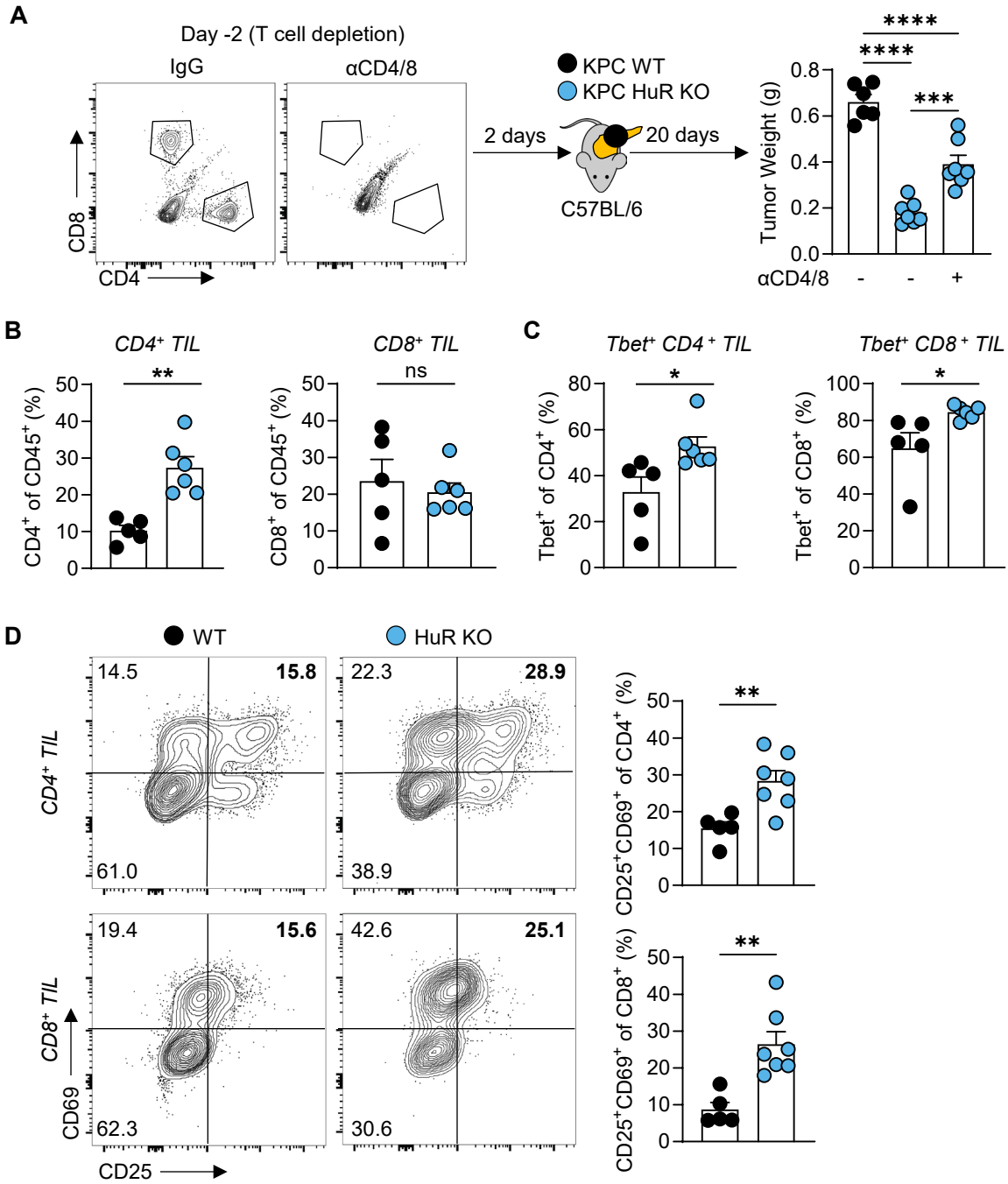

Figure 3. **HuR-dependent growth of PDAC is immune mediated *in vivo***

(**A**) Representative flow cytometry illustrating enumerating T cells in host spleens treated with IgG or αCD4/8 before and during orthotopic tumor implantation and summary analysis of final KPC WT and HuR-KO tumor weight in host with or without T cell depletion (n = 6) .

(**B**) Summary analysis enumerating tumor infiltrating lymphocytes (TIL) in orthotopic KPC WT and HuR-KO tumors (n = 5).

(**C**) Summary data depicting CD4 and CD8 T-cell Tbet$^+$ percentages and (**D**) representative flow cytometry plot and summary data depicting CD25 and CD69 phenotypic states on CD4 and CD8 T cells as in (**B**).

Error bars represent standard error of the mean. *P < 0.05; **P < 0.01; ***P < 0.005; ****P < 0.001, one-way ANOVA test (**A**), unpaired 2-tailed Student's t tests (**B,C,D**).

Figure 4

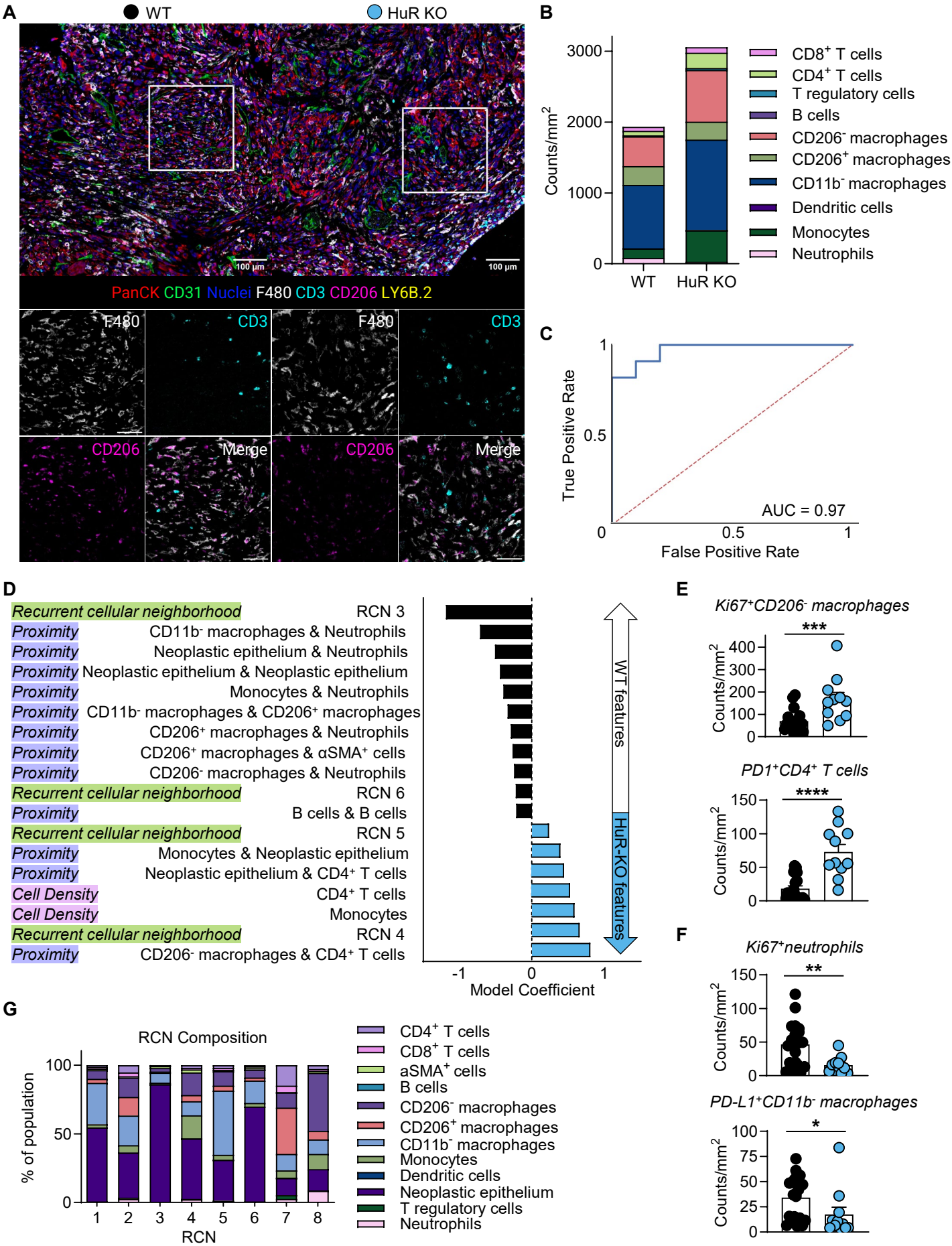
A
WT
HuR KO
100 µm
100 µm
PanCK CD31 Nuclei F480 CD3 CD206 LY6B.2
F480
CD3
F480
CD3
CD206
Merge
CD206
Merge
B
Counts/mm2
3000
2000
1000
0
WT
HuR KO
CD8+ T cells
CD4+ T cells
T regulatory cells
B cells
CD206- macrophages
CD206+ macrophages
CD11b- macrophages
Dendritic cells
Monocytes
Neutrophils
C
True Positive Rate
False Positive Rate
AUC = 0.97
0
0.5
1
D
Recurrent cellular neighborhood RCN 3
Proximity CD11b- macrophages & Neutrophils
Proximity Neoplastic epithelium & Neutrophils
Proximity Neoplastic epithelium & Neoplastic epithelium
Proximity Monocytes & Neutrophils
Proximity CD11b- macrophages & CD206+ macrophages
Proximity CD206+ macrophages & Neutrophils
Proximity CD206+ macrophages & αSMA+ cells
Proximity CD206- macrophages & Neutrophils
Recurrent cellular neighborhood RCN 6
Proximity B cells & B cells
Recurrent cellular neighborhood RCN 5
Proximity Monocytes & Neoplastic epithelium
Proximity Neoplastic epithelium & CD4+ T cells
Cell Density CD4+ T cells
Cell Density Monocytes
Recurrent cellular neighborhood RCN 4
Proximity CD206- macrophages & CD4+ T cells
WT features
HuR-KO features
-1
0
1
Model Coefficient
E
Ki67+CD206- macrophages
***
Counts/mm2
400
300
200
100
0
PD1+CD4+ T cells
****
150
100
50
0
F
Ki67+neutrophils
**
150
100
50
0
PD-L1+CD11b- macrophages
*
100
75
50
25
0
G
RCN Composition
% of population
100
50
0
1
2
3
4
5
6
7
8
RCN
CD4+ T cells
CD8+ T cells
aSMA+ cells
B cells
CD206- macrophages
CD206+ macrophages
CD11b- macrophages
Monocytes
Dendritic cells
Neoplastic epithelium
T regulatory cells
Neutrophils

Figure 4. **HuR limits T cell infiltration and activation, promoting an immunosuppressive and myeloid-driven TME landscape**

(**A**) Representative pseudo-colored mIHC images showing CD206, F4/80 (macrophages), and CD3 (T cells) in KPC WT tumors (left) and in HuR-KO tumors (right) and (**B**) summary data depicting averaged immune cell density in KPC WT (n=4) and HuR-KO tumors (n = 4).

(**C**) ROC curve with corresponding AUC for the machine learning model.

(**D**) Model coefficients for the top 18 features that drove the machine learning model to predict tumor genotype WT (black) or HuR-KO (blue). Features are ranked by importance of TME feature type to distinguish tumor genotype.

(**E**) Summary data depicting densities of $Ki67^{+}CD206^{-}$ macrophages and $PD1^{+}CD4^{+}$ T cells and (**F**) summary data depicting densities of $Ki67^{+}$neutrophils and PD-$L1^{+}$ $CD11b^{-}$ macrophages in KPC WT (n= 20 tissue regions) and HuR-KO tumors (n = 11 tissue regions).

(**G**) Stacked bar chart showing the average cellular composition of each of eight RCNs.

Error bars represent standard error of the mean. *P < 0.05; **P < 0.01; ***P < 0.005; ****P < 0.001, Mann–Whitney U-test to determine statistical significance (**E,F**).

Figure 5

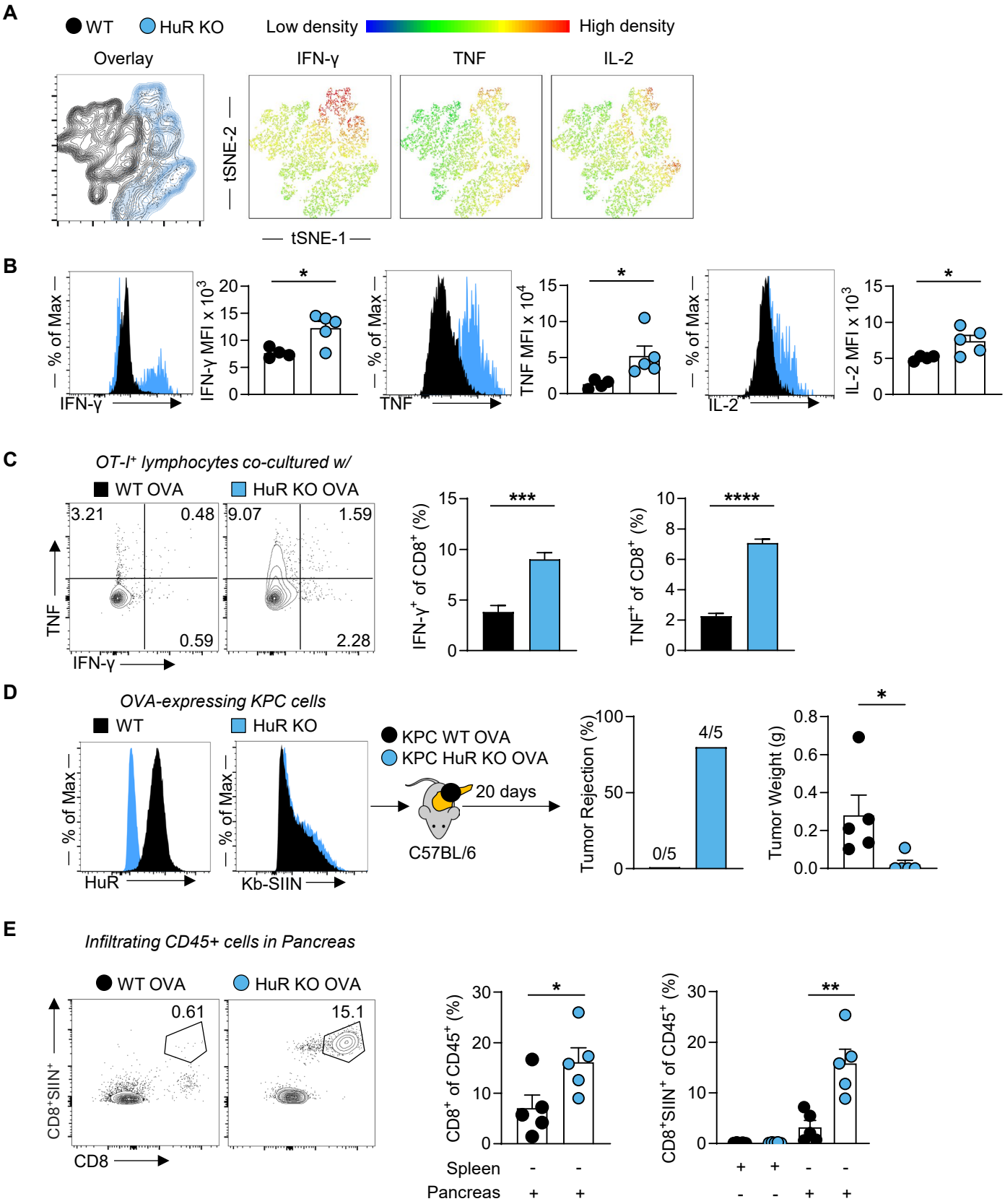
A
WT
HuR KO
Low density
High density
Overlay
IFN-γ
TNF
IL-2
tSNE-2
tSNE-1
B
% of Max
IFN-γ
IFN-γ MFI x 10^3
TNF
TNF MFI x 10^4
IL-2
IL-2 MFI x 10^3
C
OT-I+ lymphocytes co-cultured w/
WT OVA
HuR KO OVA
3.21
0.48
0.59
9.07
1.59
2.28
TNF
IFN-γ
IFN-γ+ of CD8+ (%)
TNF+ of CD8+ (%)
D
OVA-expressing KPC cells
WT
HuR KO
HuR
Kb-SIIN
KPC WT OVA
KPC HuR KO OVA
20 days
C57BL/6
Tumor Rejection (%)
0/5
4/5
Tumor Weight (g)
E
Infiltrating CD45+ cells in Pancreas
WT OVA
HuR KO OVA
0.61
15.1
CD8+SIIN+
CD8
CD8+ of CD45+ (%)
CD8+SIIN+ of CD45+ (%)
Spleen
Pancreas

<u>Figure 5</u>. HuR restricts the function and infiltration CD4 and CD8 T cells in PDAC

(**A**) Concatenated single-cell overlay and colorimetric density tSNE based depiction of the indicated proteins by flow cytometry, and (**B**) representative and summary quantification of cytokines following *ex vivo* stimulation of isolated $CD4^+$ T cells from KPC WT and HuR-KO tumors (n = 5).

(**C**) Representative flow cytometry plot and summary data depicting cytokine productions of OT-I $CD8^+$ T cells co-cultured with KPC WT OVA or KPC HuR-KO OVA tumor cells (n = 3).

(**D**) Representative flow cytometry plot depicting HuR expression and Kb-SIIN staining of KPC WT OVA or KPC HuR-KO OVA tumor cells prior to orthotopic implantation, and summary data of tumor rejection rate and final tumor weight at day 20. (**E**) Representative flow cytometry plot and summary data enumerating spleen and pancreas infiltrating $CD8^+$ T cells and $SIIN^+$ $CD8^+$ T cells from KPC WT OVA and KPC HuR-KO OVA tumor-bearing mice (n = 5).

Error bars represent stand deviation (**C**) and standard error of the mean (**B,D,E**). *$P < 0.05$; **$P < 0.01$; ***$P < 0.005$; ****$P < 0.001$, unpaired 2-tailed Student's t tests.

Figure 6

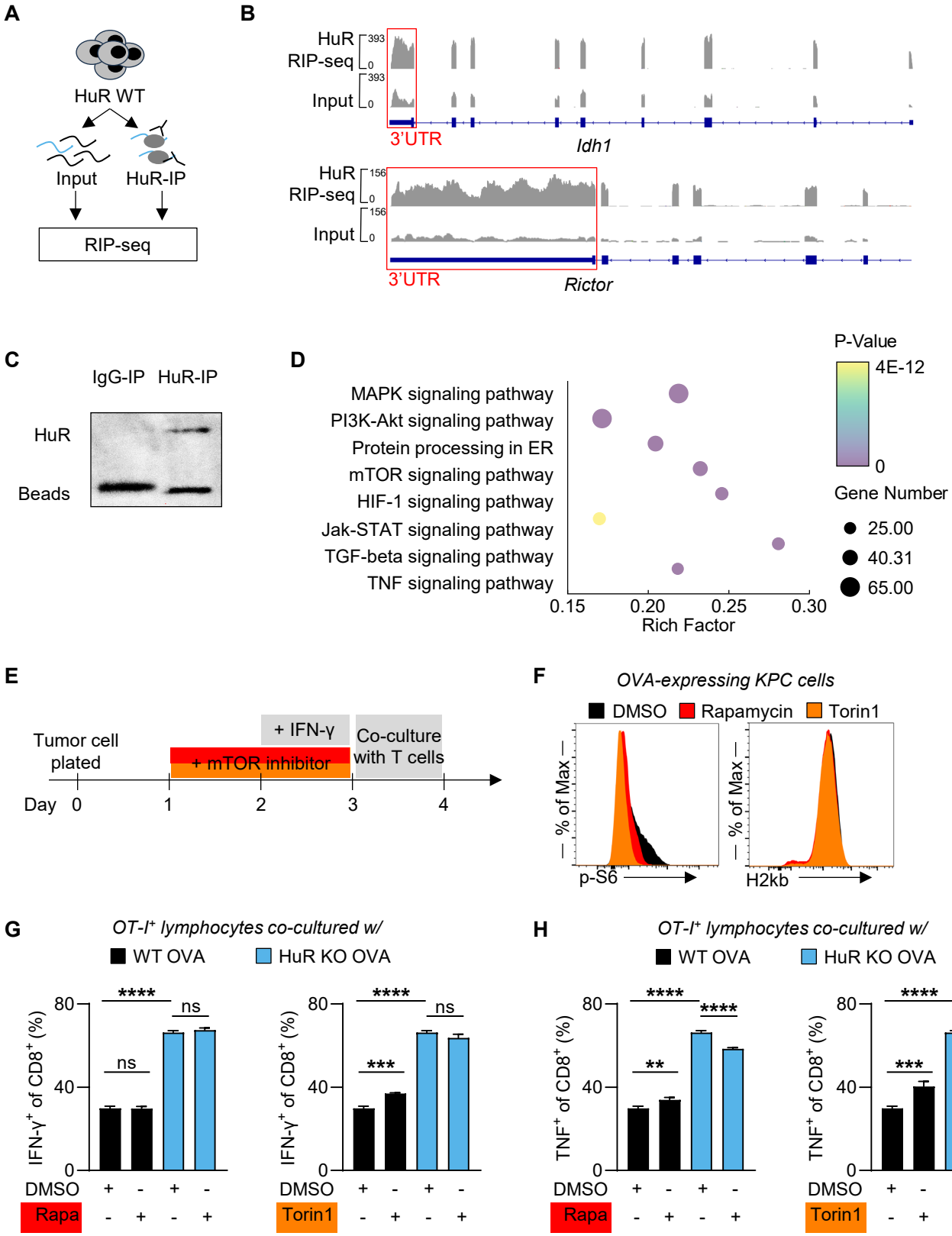
A
HuR WT
Input
HuR-IP
RIP-seq
B
HuR RIP-seq
Input
3'UTR
Idh1
Rictor
C
IgG-IP
HuR-IP
HuR
Beads
D
MAPK signaling pathway
PI3K-Akt signaling pathway
Protein processing in ER
mTOR signaling pathway
HIF-1 signaling pathway
Jak-STAT signaling pathway
TGF-beta signaling pathway
TNF signaling pathway
Rich Factor
P-Value
4E-12
0
Gene Number
25.00
40.31
65.00
E
Tumor cell plated
+ IFN-γ
+ mTOR inhibitor
Co-culture with T cells
Day
F
OVA-expressing KPC cells
DMSO
Rapamycin
Torin1
% of Max
p-S6
H2kb
G
OT-I+ lymphocytes co-cultured w/
WT OVA
HuR KO OVA
IFN-γ+ of CD8+ (%)
DMSO
Rapa
Torin1
H
TNF+ of CD8+ (%)

Figure 6. **HuR stabilizes anabolic transcripts and metabolic pathways**

(**A**) Schematic depicting RIP-seq process to identify HuR-bound transcript (n = 3). (**B**) RIP-seq reads genome alignment plot to *IDH1 and Rictor* loci (3'UTR region highlighted with red box). (**C**) Representative immunoblot validation of HuR pulldown in KPC cells in comparison to IgG control. (**D**) Summary depiction of enrichment scores (RichFactor) of KEGG pathways with transcripts comparatively enriched in HuR-IP samples.

(**E**) Schematic depicting the pre-treatment of tumor cells with mTOR inhibitors (Rapamycin and Torin1) and IFN-γ before co-culture with OT-I T cells. (**F**) Representative flow cytometry plot depicting *p*-S6 and H2-Kb staining of KPC WT OVA cells after mTOR inhibitors and IFN-γ treatments. (**G**, **H**) Summary data depicting cytokine productions of OT-I $CD8^+$ T cells co-cultured with pre-treated KPC WT OVA or KPC HuR-KO OVA tumor cells (n = 3).

Error bars represent stand deviation (**G**, **H**). *P < 0.05; ***P < 0.005; ****P < 0.001, one-way ANOVA test.

Figure 7

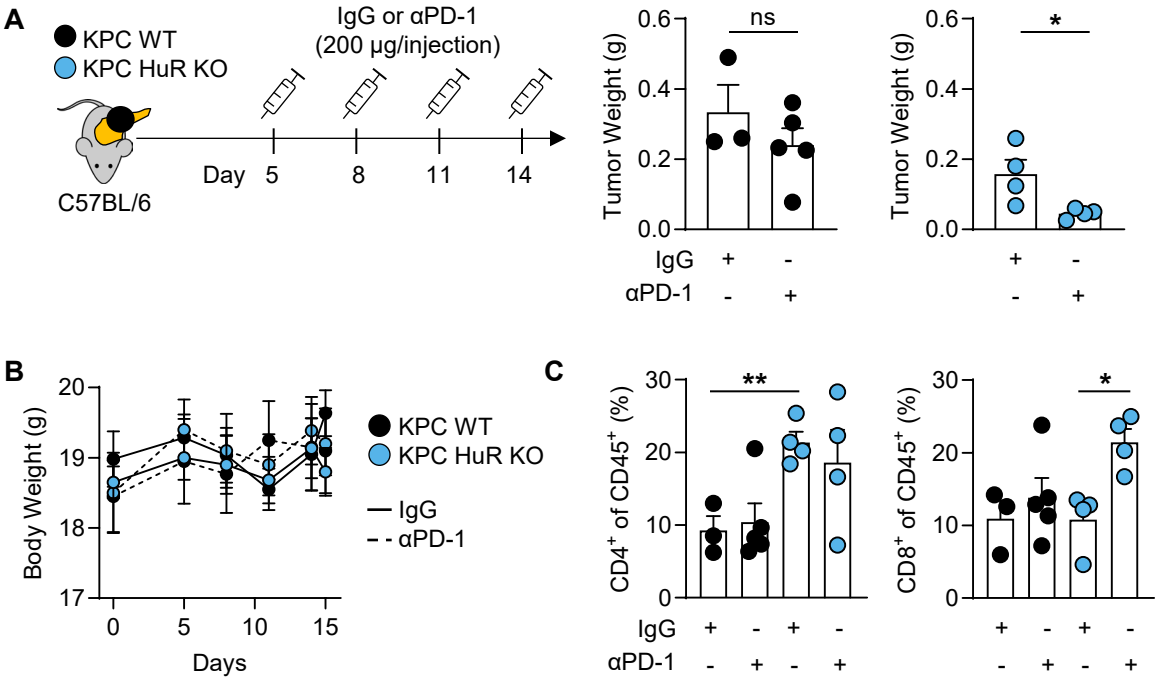

Figure 7. **PDAC resistance to immune checkpoint blockade is dependent on HuR**

(**A**) Schematic for αPD-1 treatment on KPC tumor bearing mice, and summary data on final tumor weight at day15. (**B**) Body weight of mice in (**A**) by group tracked over time (n = 4).

(**C**) Summary analysis enumerating tumor infiltrating lymphocytes (TIL) of KPC WT and HuR-KO tumors in mice received IgG or αPD-1 treatment in (**A**).

Error bars represent standard error of the mean. *P < 0.05; **P < 0.01, unpaired 2-tailed Student's t tests (**A**), one-way ANOVA test (**C**).

Supplement Figure 1

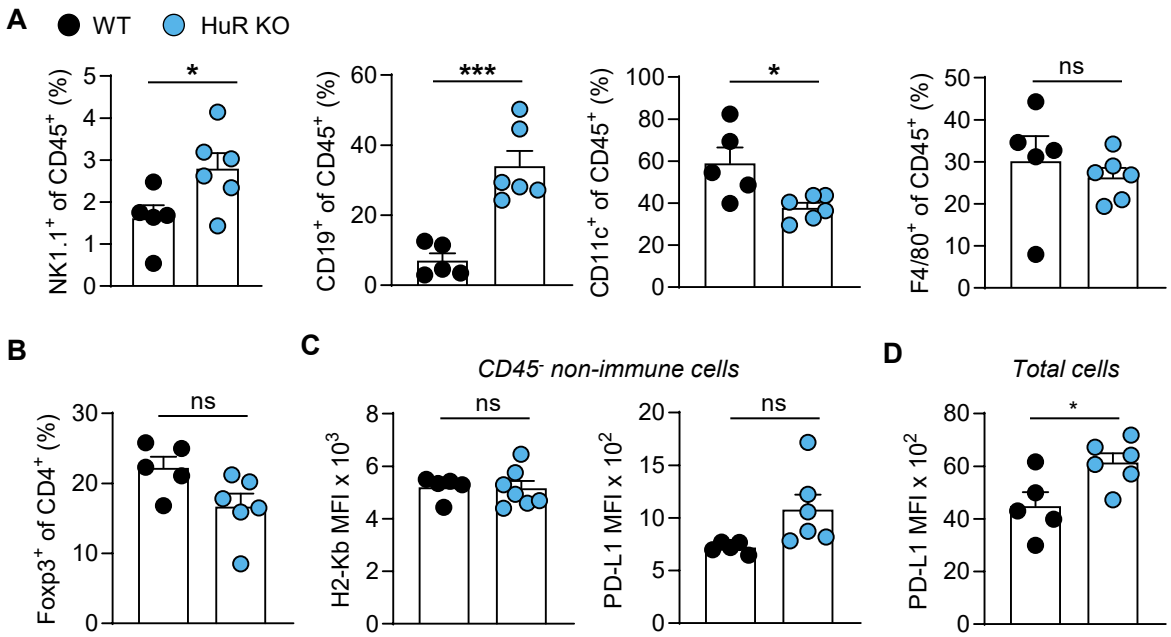

<u>Supplement Figure 1</u>. Tumor-intrinsic HuR mediates immune composition in the PDAC TME.

(**A**) Summary analysis enumerating tumor infiltrating NK cells, B cells, dendritic cells, macrophages, and (**B**) Foxp3$^+$ CD4 T-cell percentages. (**C**) Summary data depicting H2-kb and PD-L1 expression on non-immune cells, and (**D**) PD-L1 expression on all cells in orthotopic KPC WT and HuR-KO tumors (n = 5).

Error bars represent standard error of the mean. *P < 0.05; ***P < 0.005, unpaired 2-tailed Student's t tests.

Supplement Figure 2

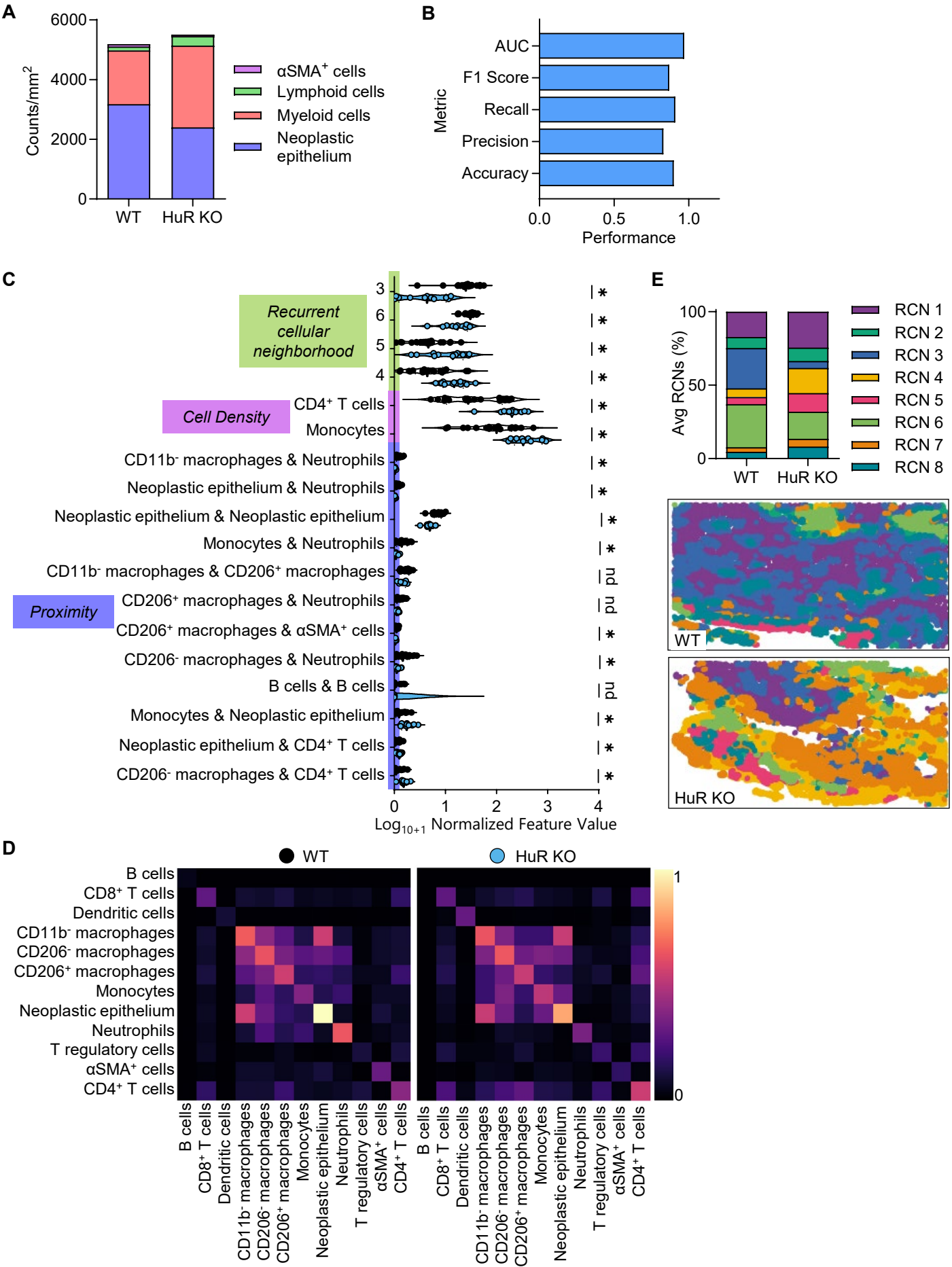

<u>Supplement Figure 2</u>. HuR limits T cell infiltration and activation, promoting an immunosuppressive and myeloid-driven TME landscape

(**A**) Summary data depicting average stromal, immune, and neoplastic epithelium cell density in KPC WT (n=4) and HuR-KO tumors (n = 4).

(**B**) Bar chart showing performance metrics for the machine learning model. (**C**) Violin plot showing the normalized values of the top 18 features driving the model. Features are organized by type on y-axis and $\log_{10+1}$ normalized values are shown on the x-axis.

(**D**) Heatmaps showing average normalized frequency of spatial proximities between two cell types for each tumor group.

(**E**) Summary data showing average fraction of RCNs present in KPC WT (n=4) and HuR-KO (n=4) tumors and scatterplot reconstructions of representative tissue regions with each cell colored by its RCN designation.

Error bars represent standard error of the mean. *$P < 0.05$, Mann–Whitney U-test to determine statistical significance (**C**).

Supplement Figure 3

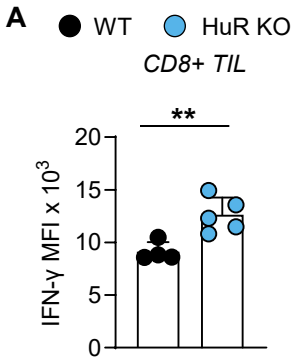

<u>Supplement Figure 3</u>. HuR restricts the function and infiltration CD4 and CD8 T cells in PDAC

(**A**) Summary quantification of IFN-γ production following *ex vivo* stimulation of isolated CD8+ T cells from KPC WT and HuR-KO tumors (n = 5).

Error bars represent standard error of the mean. **P < 0.01, unpaired 2-tailed Student's t tests.

Supplement Figure 4

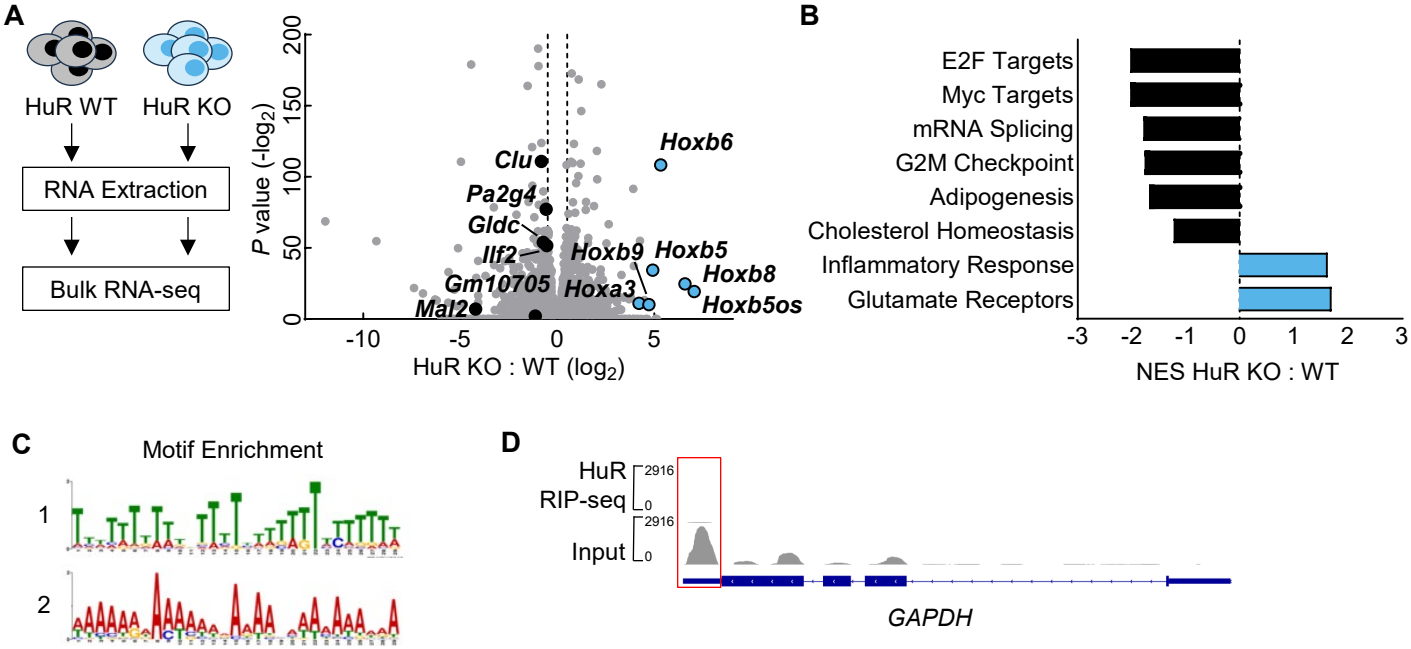

<u>Supplement Figure 4</u>. HuR stabilizes anabolic transcripts and metabolic pathways

(**A**) Schematic and volcano plot depicting whole-transcriptomic changes between KPC WT and KPC HuR-KO tumor cells (n = 3). (**B**) Summary depiction of normalized enrichment scores (NES) of gene-sets with transcripts comparatively enriched or lost between indicated groups.

(**C**) Top 2 motif enrichment sequences from HuR-IP targets. (**D**) RIP-seq reads genome alignment plot to *GAPDH* locus (3'UTR region highlighted with red box).

FDR q-value < 0.05, weighted Kolmogorov–Smirnov statistic test (**B**).

Supplement Table 1. Antibody information for flow cytometry staining

Marker	Clone	Fluorescence
CD11c	N418	BV650
CD19	1D3	BV711
CD25	PC61	BV421
CD4	RM4-5	PCP-Cy5.5
CD4	RM4-5	BUV805
CD45	30-F11	AF700
CD62L	MEL-14	BUR395
CD69	H1.2F3	APC-Cy7
CD8	53-6.7	FITC
CD8	53-6.7	APC-Cy7
CD90.2	53-2.1	BV786
F4/80	BM8	BV421
FasL	MFL3	PE
Foxp3	FJK-16s	PE
GranzB	NGZB	PE
IFNg	XMG1.2	APC
IL-2	JES6-5H4	FITC
Ki67	SolA15	BUV805
H2-kb	AF6-88.5	FITC
I-A,E	M5/114.15.2	APC-Cy7
NK1.1	PK136	PE-Cy7
PD-1	RPM1-30	APC
PD-L1	MIH5	APC
TBET	4B10	PE-Cy7
Tim3	5D12	BV650
TNF	MP6-XT22	BV421
LiveDead		Aqua

Supplement Table 2. **Antibody information for mIHC staining**

Primary Antibody	Clone	Supplier	Catalog Number
TBET	EPR9301	Ab150440	Abcam
MHCII	M5/144.15.2	14-5321-82	Thermofisher Scientific/eBioscience
CD3	SP7	RM9107S	Fisher/Epredia
CD4	D7D2Z	25229	Cell Signaling Technology
CD19	D4V4B	90176	Cell Signaling Technology
B220	RA3-6B2	550286	BD Bioscience
PD1	D7D5W	84651	Cell Signaling Technology
FOXP3	FJK16S	14-5773-82	Invitrogen
PDL1	E1L3N	13684	Cell Signaling Technology
LY6B.2	7/4	CL8993AP	Cedarlane
CD11C	D1V9Y	97585	Cell Signaling Technology
CD8	4SM15	14-0808-82	Thermofisher Scientific/eBioscience
CD206	E6T5J	24595	Cell Signaling Technology
Ly6G	1A8	551459	BD Bioscience
F4/80	D2S9R	70076	Cell Signaling Technology
CD31	SZ31	DIA-310	Dianova
CD11B	EPR1344	ab133357	Abcam
aSMA	Polyclonal	ab5694	Abcam
Ki67	Polyclonal	ab15580	Abcam
PanCK	Polyclonal	ab9377	Abcam
Histone H3	D1H2	4499	Cell Signaling Technology

Supplement Table 3. **Gating strategies for lineage assignment in mIHC**

Lymphoid cells	$CD8^+$ T cells	$CD3^+$ $CD8^+$
	$CD4^+$ T cells	$CD3^+$ $CD8^-$ $FOXP3^-$
	T regulatory cells	$CD3^+$ $CD8^-$ $FOXP3^+$
	B cells	$CD3^-$ $CD8^-$ $F480^-$ $CD11B^-$ $B220^+$
Myeloid cells	(M1-like) $CD206^-$ macrophages	$CD3^-$ $CD8^-$ $CD11B^+$ $LY6G^-$ $LY6B2^-$ $CD31^-$ $F480^+$ $CD206^-$
	(M2-like) $CD206^+$ macrophages	$CD3^-$ $CD8^-$ $CD11B^+$ $LY6G^-$ $LY6B2^-$ $CD31^-$ $F480^+$ $CD206^+$
	$CD11b^-$ macrophages	$CD3^-$ $CD8^-$ $CD11B^-$ $CD11C^-$ $LY6G^-$ $LY6B2^-$ $CD206^-$ $CD31^-$ $F480^+$
	Dendritic cells	$CD3^-$ $CD8^-$ $F480^-$ $B220^-$ $CD11c^+$ $MHC\text{-}II^+$
	Monocytes	$CD3^-$ $CD8^-$ $F480^-$ $CD11C^-$ $LY6B2^-$ $LY6G^-$ $MHCII^-$ $B220^-$ $CD31^-$ $CD11b^+$
	Neutrophils	$CD3^-$ $CD8^-$ $B220^-$ $CD11C^-$ $LY6G^+$
Other cells	Neoplastic epithelium	$CD31^-$ $CD3^-$ $CD8^-$ $B220^-$ $F480^-$ $CD11B^-$ $CD11C^-$ $LY6B2^-$ $LY6G^-$ $PanCK^+$
	αSMA^+ fibroblasts	$CD3^-$ $CD8^-$ $B220^-$ $PanCK^-$ $CD11B^-$ $CD11C^-$ $LY6G^-$ $LY6B2^-$ $F480^-$ $CD31^-$ αSMA^+